Neuron
Article

Layer-Specific GABAergic Control of Distinct Gamma Oscillations in the CA1 Hippocampus

Bálint Lasztóczi[1,*] and Thomas Klausberger[1,2,*]
[1]Department of Cognitive Neurobiology, Center for Brain Research, Medical University of Vienna, Spitalgasse 4, A-1090, Vienna, Austria
[2]Anatomical Neuropharmacology Unit, Department of Pharmacology, Medical Research Council, Oxford University, OX1 3TH, Oxford, UK
*Correspondence: balint.lasztoczi@meduniwien.ac.at (B.L.), thomas.klausberger@meduniwien.ac.at (T.K.)
http://dx.doi.org/10.1016/j.neuron.2014.01.021

SUMMARY

The temporary interaction of distinct gamma oscillators effects binding, association, and information routing. How independent gamma oscillations are generated and maintained by pyramidal cells and interneurons within a cortical circuit remains unknown. We recorded the spike timing of identified parvalbumin-expressing basket cells in the CA1 hippocampus of anesthetized rats and simultaneously detected layer-specific gamma oscillations using current-source-density analysis. Spike timing of basket cells tuned the phase and amplitude of gamma oscillations generated around stratum pyramidale, where basket cells selectively innervate pyramidal cells with GABAergic synapses. Basket cells did not contribute to gamma oscillations generated at the apical tuft of pyramidal cells. This gamma oscillation was selectively modulated by a subset of local GABAergic interneurons and by medial entorhinal cortex layer 3 neurons. The generation of independent and layer-specific gamma oscillations, implemented onto hippocampal pyramidal cells along their somato-dendritic axis, can be explained by selective axonal targeting and precisely controlled temporal firing of GABAergic interneurons.

INTRODUCTION

The mammalian brain generates a multitude of coexisting electrical oscillations that, by providing a multiplexed temporal framework for circuit operations, support a variety of cognitive functions (Buzsáki and Draguhn, 2004). In particular, neuronal oscillations in the gamma frequency range (30–100 Hz) are instrumental in sensory processing (Cardin et al., 2009), attentional selection (Gregoriou et al., 2009), and memory storage and retrieval (Lisman and Idiart, 1995; Montgomery and Buzsáki, 2007) through coordinating cell assemblies (for reviews see Colgin and Moser, 2010; Lisman and Jensen, 2013).

An increasing amount of evidence reveals that the label "gamma frequency" covers a vast diversity of different oscillations (Belluscio et al., 2012; Bragin et al., 1995; Scheffer-Teixeira et al., 2012) that may or may not share mechanisms and functional roles (Colgin et al., 2009; Csicsvari et al., 2003; Jackson et al., 2011; Mann and Mody, 2010; Middleton et al., 2008; Ray and Maunsell, 2010). Traditionally, the different hippocampal gamma oscillations have been discriminated primarily on the basis of their frequency (e.g., fast and slow gamma oscillations), but they are also differentially amplitude modulated by the hippocampal theta oscillation (5–12 Hz) (Belluscio et al., 2012; Bragin et al., 1995; Canolty et al., 2006; Tort et al., 2008), a feature that has been suggested to support the segregated flow of information across different pathways (Akam and Kullmann, 2010; Colgin et al., 2009; Tort et al., 2009). In addition to this temporal segregation by theta oscillation, gamma oscillations were found to have distinct amplitude distributions in hippocampal input layers (Belluscio et al., 2012; Fernández-Ruiz et al., 2012; Scheffer-Teixeira et al., 2012; Tort et al., 2008), where axon terminals of distinct origin innervate different subcellular domains of pyramidal cells.

How does this intricate system of oscillations emerge from neuronal circuits? The mechanisms of gamma generation have been studied in detail using in vitro models (Fisahn et al., 1998; Whittington et al., 1995). These studies revealed that in hippocampal slices parvalbumin-expressing (PV+) basket cells, innervating the somata and proximal dendrites of pyramidal cells, are the key players in the genesis of pharmacologically evoked gamma frequency rhythms (Fisahn et al., 2004; Gulyás et al., 2010; Mann et al., 2005). The contribution of PV+ basket cells to hippocampal gamma oscillations in vivo (Csicsvari et al., 2003) is more controversial, as in both CA1 and CA3, gamma oscillation amplitudes increase on the peak of the theta cycle (Bragin et al., 1995; Colgin et al., 2009; Lasztóczi et al., 2011; Soltesz and Deschênes, 1993; Stumpf, 1965; Tort et al., 2009), whereas PV+ basket cells preferentially fire on the descending phase (Klausberger et al., 2003; Lapray et al., 2012; Tukker et al., 2013; Varga et al., 2012) and are not the GABAergic cell type strongest coupled to gamma oscillations (Tukker et al., 2007). Although network gamma frequencies can be toggled pharmacologically under some conditions (Mann and Mody, 2010; Middleton et al., 2008), the coexistence of diverse gamma oscillations in vivo contrasts the unimodality observed in vitro, suggesting that models based on a single cell type may not fully account for the complexity of intact systems (Jackson et al., 2011; Middleton et al., 2008).

The diversity of GABAergic cell types with input-layer-specific axonal and dendritic distributions and cell-type-specific theta phase firing preference (reviewed in Klausberger and Somogyi, 2008) represents a hallmark of the hippocampus and cortex.

Could the diversity of GABAergic cells be involved in the generation of independent gamma oscillations occurring in the same structure? To address this, we concurrently recorded firing of identified PV+ basket cells, and local field potentials (LFPs) from multiple input layers in the CA1 area of the rat hippocampus in vivo. Due to volume conduction, LFPs at any location are considered an unknown mixture of extracellular potentials originating from different, potentially distant sources (Buzsáki et al., 2012; Kajikawa and Schroeder, 2011). To gain insight into the nature, intensity, and temporal dynamics of localized electrical processes, we analyzed the spike timing relative to current-source-density (CSD) traces, which, unlike the LFP, are largely devoid of volume-conducted components.

RESULTS

Layer- and Theta-Phase-Dependent Segregation of Hippocampal CSD Gamma Oscillations

To explore the spatiotemporal organization of distinct gamma oscillations, we simultaneously recorded LFP from 16 linearly arranged sites on a single-shank silicon probe with 100 μm contact spacing, stereotactically inserted approximately perpendicular to the input layers of the dorsal CA1 hippocampus of anaesthetized rats (Figure 1; Figure S1 available online). In these experiments (n = 37), the positioning of the probe was guided by variations in the electrophysiological signals to cover all input layers of the CA1 and was confirmed by histological analysis (Figures 2B and S1A). We analyzed gamma oscillations during theta oscillations. LFP recordings from stratum pyramidale confirmed earlier observations on the preferential occurrence of transient gamma oscillations on the peak of the theta cycle (Figures 1A and S1B) (Bragin et al., 1995). However, dynamics of more localized CSD recordings revealed theta rhythmic alternation of CSD gamma oscillations in stratum pyramidale and lacunosum-moleculare (Figures 1A and S1B), a phenomenon inconsistent with a single gamma oscillator. CSD gamma oscillations in the pyramidal layer (Figure 1A, red shading) were found to be enhanced on the trough of theta oscillations and appeared to have higher frequency than CSD gamma oscillations in stratum lacunosum-moleculare (Figure 1A, blue shading), which occurred mostly on theta peaks. The similar frequency and theta modulation of LFP gamma oscillations in stratum pyramidale and LFP and CSD gamma oscillation in stratum lacunosum-moleculare (Figures 1B and S1B) imply that LFP in the pyramidal layer, which has been the most frequent way of detecting hippocampal gamma oscillations, is dominated by volume-conducted gamma oscillations from elsewhere, most likely from stratum lacunosum-moleculare.

We analyzed CSD (or LFP) gamma oscillation amplitude as a function of input layer, frequency (20–100 Hz), and theta phase (from pyramidal layer LFP; Figure 1B). This analysis (n = 22 for CSD, and n = 6 for LFP) showed that CSD in stratum lacunosum-moleculare was dominated by an ~30 Hz gamma oscillation waxing and waning in concert with the peak of the theta cycle (Figure 1B, right, filled blue arrowhead), while pyramidal layer CSD was dominated by a faster, ~50 Hz gamma oscillation that was preferentially activated around the trough of the theta cycle (Figure 1B, right, filled red arrowhead). These characteristic patterns were not restricted to strata pyramidale and lacunosum-moleculare, but extended into stratum oriens and the proximal ~200 μm of the stratum radiatum (the perisomatic zone) and into the molecular layer of the dentate gyrus, the distal part of the stratum radiatum, and occasionally the alveus (distal dendritic zone), respectively (Figures 1B, 2E, and 7C). In CSD analysis, patterns characteristic of pyramidal layer and stratum lacunosum-moleculare were not observed in stratum lacunosum-moleculare and the pyramidal layer, respectively (Figure 1B, right, open red and blue arrowheads). Thus, we define two CSD gamma oscillations, one centered on the pyramidal layer that we will call "perisomatic gamma" ($gamma_{perisomatic}$) and another localized to distal dendrites that we will call "apical tuft gamma" ($gamma_{apical\ tuft}$) oscillations. The distinct character of the two could not be revealed in LFP recordings (Figure 1B, left), and therefore, we based all further analyses of gamma oscillations on CSD analysis.

We also performed recordings with a linear 16-site silicon probe with 50 μm contact spacing inserted into the dorsal CA1 hippocampus of drug-free, head-fixed mice (n = 3). The spatiotemporal distribution of CSD gamma oscillations was qualitatively consistent with that observed in urethane-anaesthetized rats, with the gamma oscillations in strata lacunosum-moleculare and radiatum preferentially occurring on the peak and gamma oscillations around stratum pyramidale preferentially occurring on the trough/descending phase of theta oscillations (Figure 1C).

Spike-Timing of PV+ Basket Cells Is Coupled to $Gamma_{perisomatic}$ but Not $Gamma_{apical\ tuft}$

How does the activity of PV+ basket cells, reported to generate gamma oscillations in vitro, correlate with distinct hippocampal CSD gamma oscillations in space and time? We corecorded identified PV+ basket cells with extracellular glass electrodes and LFPs from the silicon probe placed nearby. Based on the characteristic enrichment of axon terminals in the pyramidal layer and its immediate vicinity (Figure 2B) and PV immunoreactivity (Figure 2C), we identified five juxtacellularly labeled CA1 cells as PV+ basket cells (Figure 2B). Dendrites of PV+ basket cells had radial orientation and spanned strata oriens and radiatum, but they extended little into stratum lacunosum-moleculare (Figure 2B) (Tukker et al., 2013). All PV+ basket cells successfully tested were immunonegative for neuropeptide Y (n = 3) and somatostatin (n = 1) and immunopositive for PV (n = 5), Erb4 (n = 1), and the α1 subunit of the $GABA_A$ receptor (n = 1).

Upon visual inspection during theta oscillations, spikes of PV+ basket cells appeared to be coincident with increased gamma oscillation amplitude in CSD recordings from the perisomatic zone (Figures 2A, 2D, and 2E). By contrast, CSD gamma oscillations in the distal dendritic zone were found to decrease in amplitude when PV+ basket cells were active (Figures 2A, 2D, and 2E). These correlations were a consequence of concerted theta phase modulation of $gamma_{perisomatic}$, $gamma_{apical\ tuft}$, and the firing of PV+ basket cells (Figures 2A, 2D, and 2E). The firing of the cell B96b (Figure 2) was significantly ($p << 0.001$; Rayleigh test; n = 4,450 spikes) biased to the descending phase of the LFP theta cycle in stratum pyramidale (mean phase angle was 326°) (Figure 2E) (Klausberger et al., 2003), when

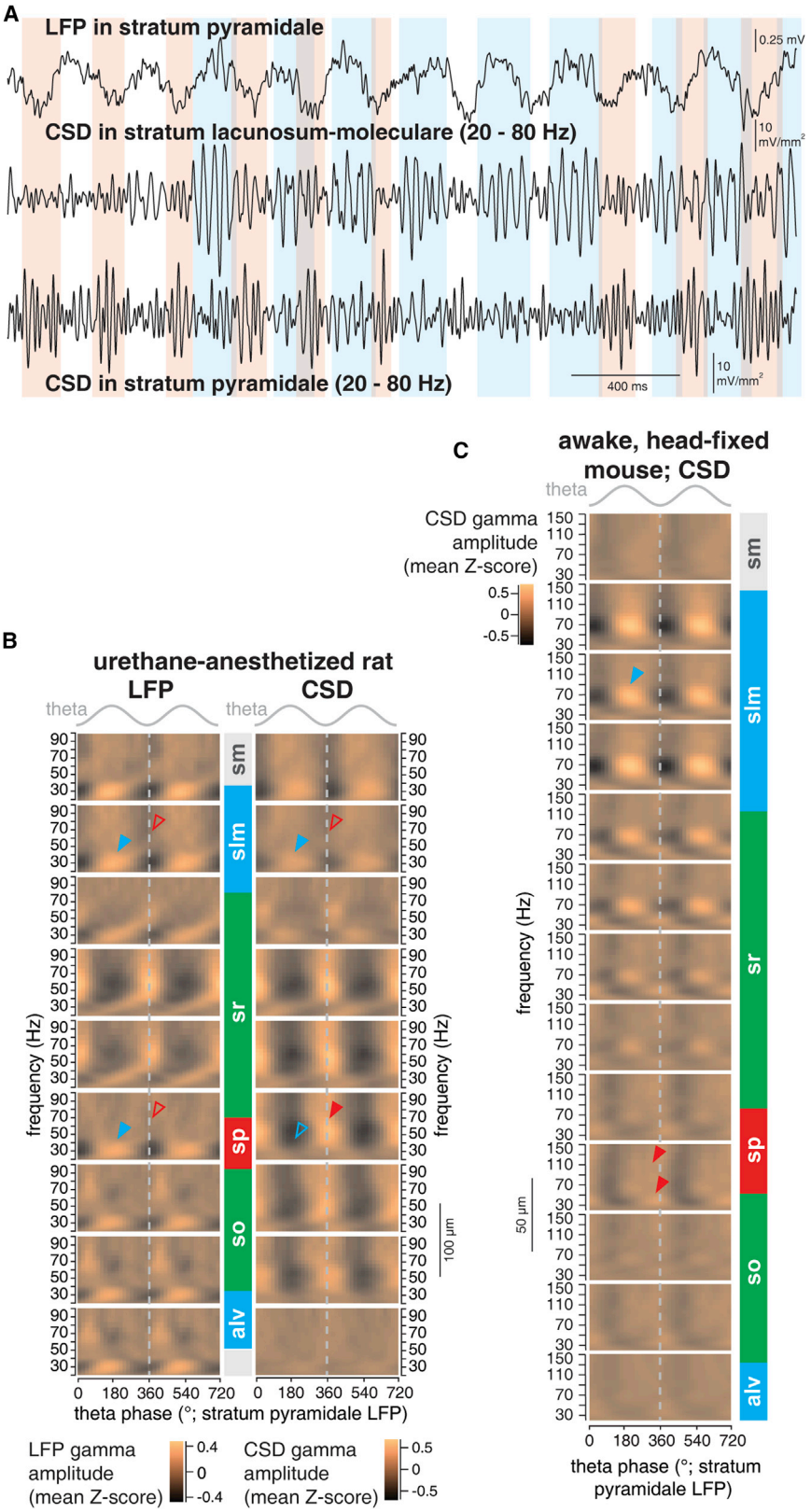

Figure 1. Two Distinct Gamma Oscillations in the Dorsal CA1

(A) Local field potential (LFP) in stratum pyramidale with concurrent theta and gamma oscillations and gamma-filtered (20–80 Hz) current-source-density (CSD) in stratum lacunosum-moleculare and stratum pyramidale recorded with a silicon probe; current source is upward. Note that CSD gamma oscillations occur on opposite phases of theta cycles in strata pyramidale and lacunosum-moleculare (red and blue shading, respectively).

(B) Cross-frequency coupling between LFP theta (stratum pyramidale) and gamma-LFP (left) or gamma-CSD (right) oscillations (mean Z-scored amplitude; color-coded), averaged from one experiment (theta oscillatory periods of 276 s cumulative duration) in a urethane-anesthetized rat. Each plot is for one silicon probe contact; CA1 layers are indicated in the middle. Theta phase modulation and spatial distribution reveal two distinct CSD gamma oscillations (right): "perisomatic gamma" (filled red arrowhead) and "apical tuft gamma" (filled blue arrowhead). Perisomatic gamma does not appear in CSD in stratum lacunosum-moleculare (slm) or in LFP in either stratum lacunosum-moleculare or pyramidale (sp; open red arrowheads), and apical tuft gamma is absent from CSD in the pyramidal layer (open blue arrowhead). Note that the LFP in stratum pyramidale is dominated by volume-conducted gamma oscillations that may originate from stratum lacunosum-moleculare (left; filled blue arrowhead).

(C) Cross-frequency coupling between LFP theta (stratum pyramidale) and gamma-CSD oscillations (mean Z-scored amplitude; color coded), averaged from one experiment (theta oscillatory periods of 652 s cumulative duration) in a drug-free, head-fixed mouse. CA1 input-layers are indicated on the right; colored, filled arrowheads point to distinct gamma oscillations. Abbreviations are as follows: alv for alveus, sm for stratum moleculare, so for stratum oriens, and sr for stratum radiatum. See also Figure S1.

gamma$_{perisomatic}$ was strong and gamma$_{apical\ tuft}$ was weak (red arrowheads in Figure 2E). Firing of the PV+ basket cells was not only positively correlated to the amplitude of gamma$_{perisomatic}$ but also the action potentials preferentially occurred on the ascending phase of CSD gamma cycles in stratum pyramidale (Figures 2A and 2F). Spikes also occurred on least preferred parts of theta cycle, coincident with strong gamma$_{apical\ tuft}$ (Figures 2A and 2D), but their timing was hardly dependent on the phase of CSD gamma oscillations in stratum lacunosum-moleculare (Figures 2A and 2F).

To quantify the coupling strength of PV+ basket cells to gamma$_{perisomatic}$ and gamma$_{apical\ tuft}$, we defined the frequency ranges occupied by these two CSD gamma oscillations based on theta phase modulation spectra (20–100 Hz; see Experimental Procedures). The center frequency for gamma$_{perisomatic}$ was significantly higher than the center frequency for gamma$_{apical\ tuft}$ (46 ± 7.2 Hz versus 29 ± 5.4 Hz; mean ±SD; $p = 0.0017$; $t_{(4)} = 7.54$; paired t test; $n = 5$), but there was a significant overlap between the two frequency ranges (Figure 3A), indicating that defining frequency ranges alone is insufficient to separate gamma oscillations. We analyzed how the phase coupling of PV+ basket cells to CSD oscillations in these two frequency ranges depend on the CA1 input layer (Figure 3B). We reasoned that the coupling strength should increase with decreasing distance to the source of oscillation to which the phase coupling is genuine. We detected significant variation of the normalized coupling strength as a function of input layer for both gamma frequency ranges ($p << 0.001$; $F_{(7,32)} = 24.89$; $n = 5$; $p << 0.001$; $F_{(7,32)} = 21.64$; $n = 5$; one-way ANOVA). Notably, the maximum of the mean vector length across layers (the normalization base) was significantly different between the two frequency ranges (0.27 ± 0.12 for gamma$_{perisomatic}$ range versus 0.15 ± 0.04 for gamma$_{apical\ tuft}$ range; mean ±SD; $p = 0.0079$; $n = 5$; Mann-Whitney U test). Consistent with genuine phase coupling to gamma$_{perisomatic}$, we observed that in its frequency range the mean vector length was higher in the perisomatic zone (black asterisks in Figure 3B; Tukey's test at $\alpha = 0.05$; see also Figures 2D–2F). However, it was the very same locations for which the phase coupling in the frequency range of gamma$_{apical\ tuft}$ was increased as well (gray asterisks in Figure 3B; Tukey's test at $\alpha = 0.05$), despite limited contribution from gamma$_{apical\ tuft}$ in these contacts (Figures 1B and 2D–2F). Indeed, the coupling strength, as measured by the mean vector length, was indicative of strong coupling to gamma$_{perisomatic}$ (0.25 ± 0.12; mean ±SD; range 0.19–0.47) but of minimal coupling to gamma$_{apical\ tuft}$ (0.037 ± 0.013; range 0.024–0.054). The difference between the coupling strengths was highly significant ($p = 0.0079$; $n = 5$; Mann-Whitney U test; Figure 3C). We also observed that the frequency range, over which strong phase coupling of PV+ basket cells to gamma$_{perisomatic}$ was observed, showed marked overlap with the frequency range, for which gamma$_{perisomatic}$ was strongly modulated by theta oscillations (compare Figures 2E and 2F, left column). Accordingly, the frequency, at which peak modulation of PV+ basket cells occurred (55 ± 15 Hz; mean ±SD; $n = 5$) was not different from the center frequency of gamma$_{perisomatic}$ ($p = 0.28$; $t_{(4)} = -1.25$; paired t test). Overall, these data demonstrate that PV+ basket cells fire strongly phase coupled to gamma oscillations generated around stratum pyramidale, but they did not contribute to gamma oscillations generated at the apical tufts.

Theta Phase Modulation of Firing and Gamma Phase Coupling of PV+ Basket Cells Explains the Waxing and Waning of Gamma$_{perisomatic}$ during the Theta Cycle

Next, we analyzed the theta phase dependence of gamma spike timing of PV+ basket cells. As an average theta cycle (~220 ms) may accommodate ~10 gamma cycles at 45 Hz, we sampled PV+ basket cell spikes from 10 theta phase bins and calculated coupling to CSD gamma oscillations within each bin separately. Significant phase coupling to gamma$_{perisomatic}$ (at $\alpha = 0.05$; Rayleigh test) with similar preferred phase (Figures 4A and S2) was observed throughout all theta phase bins. The strength of phase coupling, as measured by mean vector length spectra, however, showed marked fluctuation as a function of theta phase, having a minimum on the ascending phase, gradually increasing, and reaching peak just after the trough, followed by a rapid decline. Statistical analysis ($n = 5$ basket cells; Figure 4B1) disclosed significant variation in the strength of PV+ basket cell spike coupling to gamma$_{perisomatic}$ ($p = 0.018$; $F_{9,40} = 2.6$; $n = 5$; one-way ANOVA) but not to gamma$_{apical\ tuft}$ ($p = 0.8$; $F_{9,40} = 0.59$; $n = 5$; one-way ANOVA). The firing of PV+ basket cells was nonuniformly ($p < 0.001$; Rayleigh test; $n = 5$ cells; >500 spikes for each cell) distributed across the theta cycle, with a clear phase preference to the descending phase (mean phase angle was 334° ± 11.8°; circular mean of mean phases ± circular SD; range of means 324°–350°; mean vector length: 0.23 ± 0.10; mean ±SD; range 0.12–0.34) (Figure 4B2). The highest amplitude of gamma$_{perisomatic}$ at the trough of theta oscillations can be explained by the combination of the highest firing rate of PV+ basket cells before, and their strongest gamma phase coupling after the theta trough (Figure 4C). This indicates that during the descending theta cycle phase, the increasing firing of PV+ basket cells builds up a slightly lagging gamma synchrony that reaches its maximum after the highest firing of PV+ basket cells. On the ascending theta phase, both firing rate and gamma synchrony collapses, and an independent gamma$_{apical\ tuft}$ oscillation builds up in stratum lacunosum-moleculare.

Coupling of CA3 Pyramidal Cells to CA1 Gamma Oscillations

Next, we determined the temporal relationship between the spike timing of PV+ basket cells or CA3 pyramidal cells and the current sinks and sources of gamma oscillations in the different layers of CA1 (Figure 5A).

In three experiments with silicon probe recordings from the CA3 region of the dorsal hippocampus, we have recorded and isolated 111 units firing during theta oscillations (19 putative interneurons, 83 putative pyramidal cells, and 9 undetermined). Putative pyramidal cells were identified based on burst firing and characteristic spike shape, with a subset ($n = 23$) showing monosynaptic excitatory connection to at least one unit. Coupling of CA3 pyramidal cells to CSD gamma oscillation in the CA1 was explored by inspecting the spatial profiles of mean phase and coupling strength spectra. A subset of putative pyramidal cells ($n = 15$) displayed firing rates >2 Hz during theta oscillations (mean ±SD; 4.2 ± 2.3 Hz; range 2.02–9.78) and often

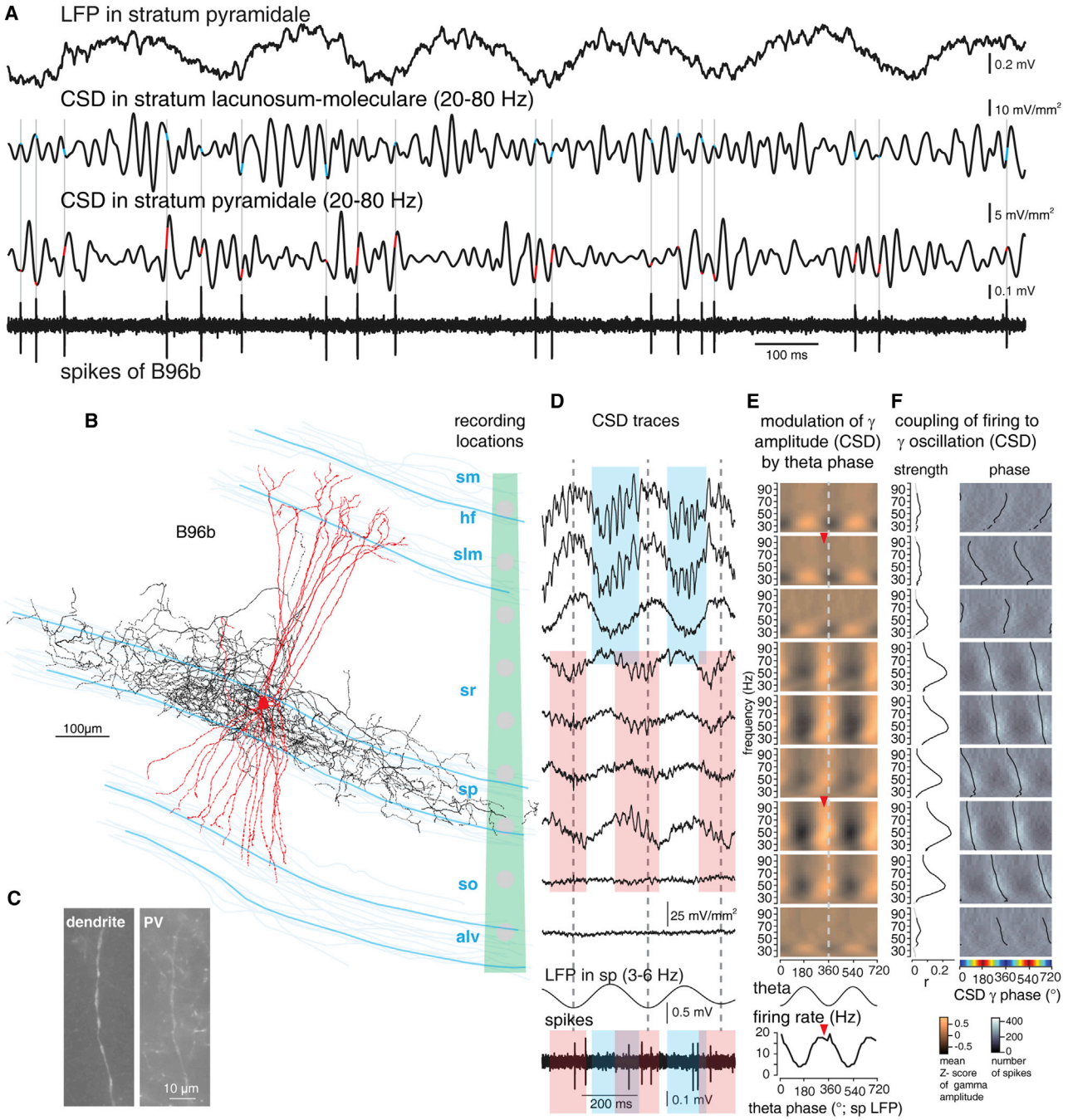

Figure 2. Spikes of an Identified Parvalbumin-Expressing Basket Cell Are Selectively Phase Coupled to $Gamma_{perisomatic}$, but Not $Gamma_{apical\ tuft}$ Oscillations

(A) Silicon probe recordings of LFP from stratum pyramidale and gamma-filtered (20–80 Hz) CSD from stratum lacunosum-moleculare and pyramidale, and extracellular (glass electrode) recording of spikes of an identified parvalbumin-expressing (PV+) basket cell (B96b). Cell firing is associated with strong CSD gamma oscillations in the pyramidal layer, and individual spikes tend to fall on the ascending phase (red; current source is upward). In stratum lacunosum-moleculare, CSD gamma oscillations are smaller during firing and spikes are evenly distributed to different phases (blue).

(B) Neurolucida reconstruction of the cell shown in (A). Soma, dendrites (red, full), and axon (black, partial) of the neurobiotin-labeled cell B96b and the position of the recording contacts (gray circles) of the silicon probe (green) are displayed.

(C) A dendrite of B96b (left) is immunopositive for parvalbumin (PV; right).

(D) CSD traces deducted from the silicon probe (top, aligned to reconstruction in [B]) and the spikes of the cell (bottom). Theta-filtered (3–6 Hz) LFP from stratum pyramidale is shown for reference; vertical dashed lines mark the troughs. The spatiotemporal extent of perisomatic and apical tuft gamma oscillations are marked by red and blue shading, respectively.

(legend continued on next page)

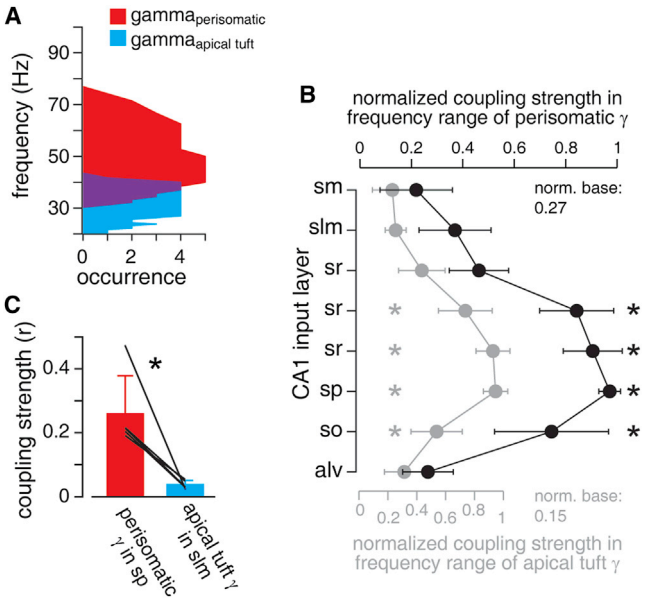

Figure 3. PV+ Basket Cells Are Selectively Phase-Coupled to the Perisomatic Gamma Oscillation

(A) Frequency distribution of perisomatic (red) and apical tuft (blue) gamma oscillations; note the significant overlap (purple).

(B) Spatial profiles of normalized coupling strength (mean vector length, r; mean ±SD) of PV+ basket cell spikes to CSD gamma oscillations, calculated over the frequency range of $gamma_{perisomatic}$ (black) or $gamma_{apical\ tuft}$ (gray). The abscissae are scaled proportional to the mean normalization base, displayed in top- and bottom-right corners. Asterisks denote significantly increased coupling (at $\alpha = 0.05$, one-way ANOVA followed by Tukey's multiple comparisons). Note that the coupling increases around the pyramidal layer even when analyzed over the frequency range of $gamma_{apical\ tuft}$.

(C) Phase coupling strength (r) of PV+ basket cell firing (n = 5) to $gamma_{perisomatic}$ (red) and $gamma_{apical\ tuft}$ (blue; mean ±SD); asterisk indicates p = 0.0079 (Mann-Whitney U test).

showed preferential phase coupling to 20–45 Hz CSD oscillations in the molecular layer of the dentate gyrus (data not shown). The remaining putative pyramidal cells (firing at 0.60 ± 0.51 Hz during theta oscillations; range 0.01–1.99 Hz) were often coupled to $gamma_{perisomatic}$. As many individual units had not enough spikes to generate meaningful coupling spectra, we pooled the corecorded units (putative pyramidal cells firing at <2 Hz) to generate spectra for the CA3 pyramidal cells as a population (n = 2,091, 3,594, and 927 spikes from 11, 40, and 17 units, in three experiments). Indeed, these spectra showed significant coupling to CA1 CSD gamma oscillations corresponding in frequency and spatial distribution to $gamma_{perisomatic}$ (Figure 5A). When averaged over the 30–70 Hz range, the normalized mean coupling strength showed significant variation with the input layer ($p = 0.0016$; $F_{8,26} = 5.32$; n = 3; one-way ANOVA) (Figure 5B).

The spikes of PV+ basket cells occurred, on average, 6.1 ms before the maximum current source in the stratum pyramidale (Figure 5C), and their coupling phase reversed across the borders to strata radiatum and oriens, consistent with a local $gamma_{perisomatic}$ current generator through GABAergic inhibition on pyramidal cell somata and return currents in strata oriens and radiatum (Figures 5C and S3). An average 8.5 ms time lag between CA3 pyramidal and CA1 PV+ basket cell firing may indicate some $gamma_{perisomatic}$ entrainment of CA1 basket cells by the CA3 input. In addition, we found that during theta oscillations, PV+ basket cell firing is associated with maximum theta current sink in the proximal part (100–250 μm) of stratum radiatum (Figure 6), where they receive a large number of excitatory synapses most likely originating from CA3 pyramidal cells (Gulyás et al., 1999; Tukker et al., 2013). Overall, these results indicate that PV+ basket cells are recruited by excitation from the CA3 area during theta oscillations.

Cellular Networks for $Gamma_{apical\ tuft}$

To test possible contributions of the dorsal medial entorhinal cortex (dMEC) to $gamma_{apical\ tuft}$ oscillations, we inserted 16 site linear silicon probes (50 μm spacing) into the dMEC (n = 3 experiments; Figure 7A) and recorded units from the layer 3 (L3) and layer 2 (L2), which give rise to fibers terminating in the stratum lacunosum-moleculare of the CA1 and the molecular layer of dentate gyrus, respectively. Simultaneously, we recorded CSD gamma oscillations in different hippocampal layers with an additional silicon probe. We recorded and isolated 133 dMEC units, including 55 putative interneurons and 63 putative excitatory cells identified based on their characteristic spike shape and autocorrelogram, with a subset (n = 24) showing functional monosynaptic excitatory connection to at least one unit; 15 cells remained unclassified. Putative projection cells in L3 preferentially fired before the peak of theta oscillations in CA1 stratum pyramidale (Figure 7B). We pooled their spikes for individual experiments and generated population coupling spectra for hippocampal CSD gamma oscillations (n = 293, 2,774, and 12,672 spikes from 6, 1, and 5 units) (Figure 7C). L3 putative projection cells showed significant coupling to 20–45 Hz CSD gamma oscillations recorded from stratum lacunosum-moleculare (Figure 7C), less coupling to CSD gamma oscillations recorded in the molecular layer of the dentate gyrus, and very little or no coupling to CSD oscillations in the stratum pyramidale. Quantitative analysis confirmed significant variation of coupling strength as a function of input layer (Figure 7D) ($p = 0.0011$; $F_{8,26} = 5.66$; n = 3 experiments; one-way ANOVA). Projection cells in L3 of dMEC preferentially fired at the peak of $gamma_{apical\ tuft}$ in stratum lacunosum-moleculare (Figure 7E), where their spikes were followed by the maximum sink after 13.2 ms. This delay (Charpak et al., 1995; Townsend et al., 2002), together with a phase reversal of coupling across the border between

(E) CSD gamma oscillation amplitude as a function of theta phase (as in Figure 1B; 377 s cumulative duration). Firing of cell B96b (bottom) coincides with perisomatic, but not apical tuft, gamma oscillations (red arrowheads indicate mean firing phase of the cell).

(F) Coupling of spike timing to CSD gamma oscillations in different layers (plots are aligned to [B]). Left shows mean vector length (r) spectra; significant values are plotted in black (Rayleigh test, $\alpha = 0.05$). Right shows spike density plots (color-coded spike count as a function of CSD oscillation phase for each frequency; two cycles are shown, maximum sink is 0° and 360° and maximum source is 180°), and mean firing phase spectra (black lines, only significant values plotted); note strongest coupling in the perisomatic zone. hf indicates hippocampal fissure.

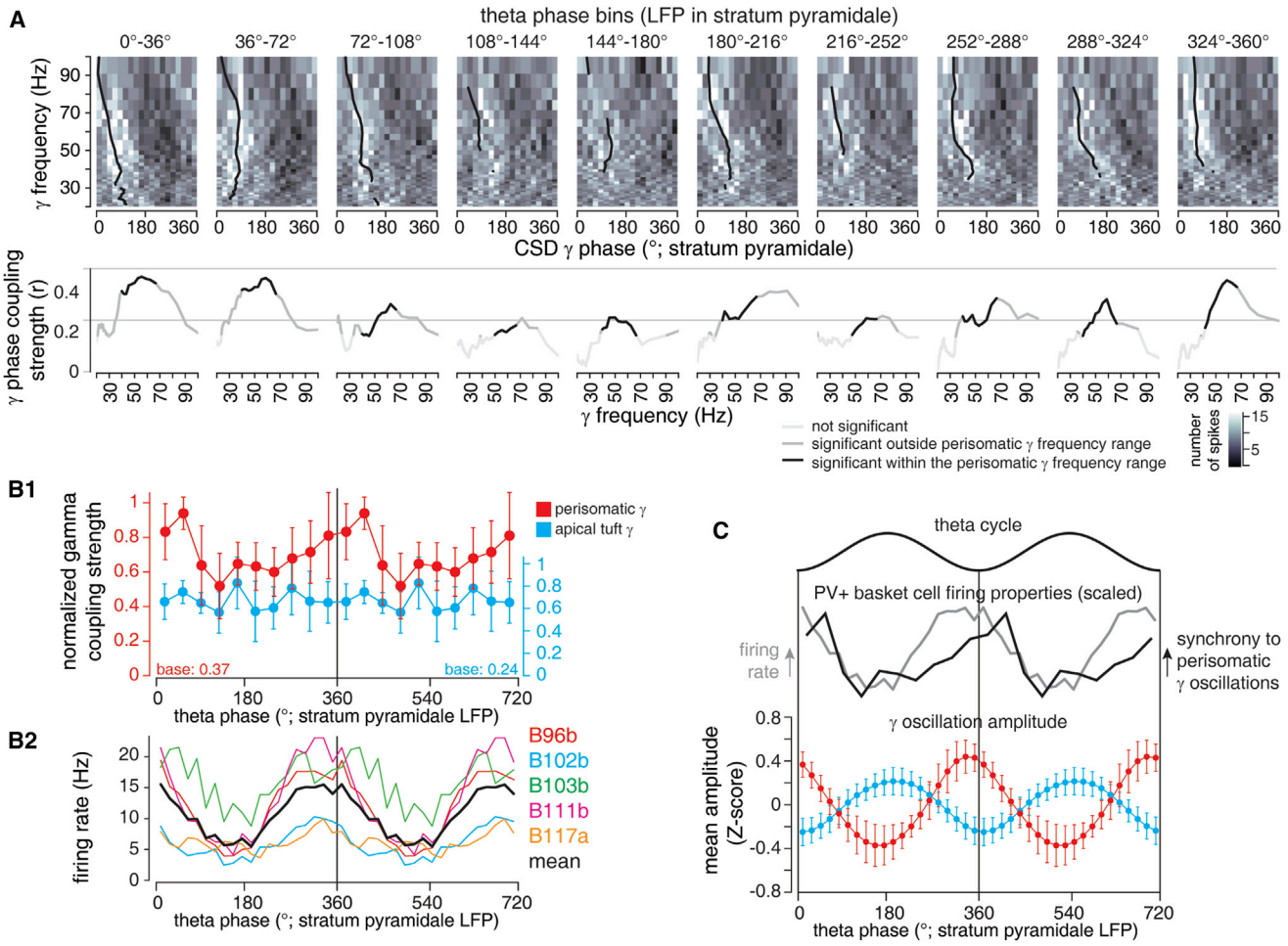

Figure 4. Phase Coupling of PV+ Basket Cells to Gamma$_{perisomatic}$, but Not Gamma$_{apical\ tuft}$ Is Theta Phase Dependent

(A) Phase coupling of spikes of a PV+ basket cell (B111b) to CSD gamma oscillations in the pyramidal layer during different phases of the LFP theta cycle. Theta cycles were divided into 10 bins (indicated above; 180° is peak), and for each bin, the number of spikes is displayed color coded as a function of CSD gamma phase for frequencies between 20 and 100 Hz (top; 0° and 180° indicate maximum sink and source, respectively). To account for unequal samples, 161 spikes were randomly selected for the analysis of each bin. Mean phase spectra (black lines) are plotted for frequencies with nonuniform spike phase distribution ($\alpha = 0.05$; Rayleigh test). Below, mean vector length spectra plotted in black (significant values inside the gamma$_{perisomatic}$ frequency range), dark gray (significant values outside this range), or light gray (values from uniform phase distributions). Note that the coupling strength, but not the preferred phase, changes as a function of theta phase.

(B1) Theta-phase-dependent fluctuation of normalized phase coupling strength (mean ±SD) of PV+ basket cell (n = 5) firing to gamma$_{perisomatic}$ (red) and gamma$_{apical\ tuft}$ (blue). Ordinates are scaled proportional to the average normalization base (maximum values shown color coded). Only coupling to gamma$_{perisomatic}$ varied significantly ($\alpha = 0.05$; one-way ANOVA).

(B2) Theta-phase-dependent fluctuation of firing rate in PV+ basket cells (all cells $p < 0.01$; $n > 500$ spikes; Rayleigh test). Individual cells are color coded; the mean is black.

(C) Theta-phase-dependent fluctuation of the amplitude of gamma$_{perisomatic}$ (red) and gamma$_{apical\ tuft}$ (blue; mean ±SD of Z-scored amplitude; variation significant for both; $\alpha = 0.05$, one-way ANOVA). The combination of theta phase modulation of PV+ basket cell firing rate (top; gray) and the strength of their phase coupling to gamma$_{perisomatic}$ (top; black; re-plotted from B) explains the waxing and waning of gamma$_{perisomatic}$. See also Figure S2.

strata radiatum and lacunosum-moleculare (Figures 7E, S3, and S4A) is consistent with L3 cells generating the current sink of hippocampal gamma$_{apical\ tuft}$.

Putative projection cells in L2 of dMEC showed a bimodal distribution with respect to their preferred theta phase (Figure 7B), with the population coupled to the trough of CA1 theta oscillations displaying little coupling to hippocampal gamma oscillations (data not shown). By contrast, the population that fired on the peak of theta (n = 910, 4,720, and 1,812 spikes from 5, 1, and 14 units in three experiments), showed significant coupling to 20–45 Hz CSD oscillations recorded from the molecular layer of dentate gyrus but only limited coupling to CSD gamma oscillations in CA1 (Figures 7C and 7D) ($p = 0.0015$; $F_{8,26} = 5.34$; $n = 3$; one-way ANOVA for the variation of the coupling strength with the CA1 input layer). Consistent with connectivity, these data indicate the independence of CA1 gamma$_{apical\ tuft}$ from gamma oscillations in the molecular layer of the dentate gyrus.

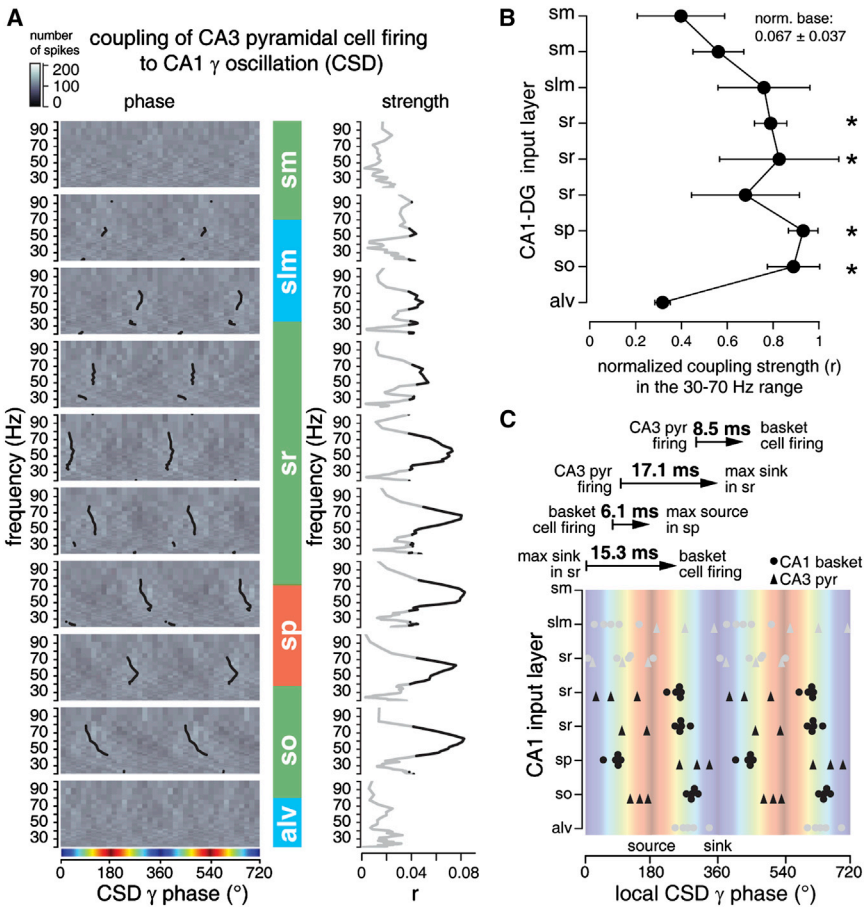

Figure 5. Temporal Dynamics of Gamma$_{perisomatic}$-Phase-Dependent Firing of CA3 Pyramidal Cells and CA1 PV+ Basket Cells

(A) Coupling of CA3 pyramidal cell spike timing to CSD gamma oscillations in different layers of CA1. All spikes attributed to putative CA3 pyramidal cells firing at <2 Hz rate from one experiment (B129c) were pooled (n = 2,091 spikes from 11 units). Left shows spike density plots (color-coded spike count as a function of CSD oscillation phase; maximum sink is 0° and 360° and maximum source is 180°) and mean firing phase spectra (black lines, only significant values plotted; Rayleigh test, α = 0.05). Right shows the corresponding mean vector length (r) spectra; significant values are plotted in black. Note increased coupling to gamma oscillations corresponding to the frequency range and layer-location of gamma$_{perisomatic}$.

(B) Spatial profile of normalized coupling strength (mean vector length, r) of CA3 pyramidal cell spikes to CA1 CSD gamma oscillations, calculated over the 30–70 Hz frequency range, corresponding to gamma$_{perisomatic}$ (mean ±SD; n = 3 experiments). Asterisks denote significantly increased coupling (at α = 0.05, one-way ANOVA followed by Tukey's multiple comparisons).

(C) Mean firing phases of PV+ basket cells (n = 5, dots) and CA3 pyramidal cells (triangles; n = 3 experiments with spikes pooled as above) are plotted for all layers relative to local CSD gamma oscillations (calculated for the frequency range of gamma$_{perisomatic}$ and 30–70 Hz for basket cells and CA3 pyramidal cells, respectively; for clarity, symbols in layers with apical tuft gamma are shown in gray and overlapping symbols are vertically displaced). Time lags displayed above the plot are calculated assuming a 45 Hz gamma cycle. See also Figure S3.

The selective entrainment of PV+ basket cells by gamma$_{perisomatic}$ in the CA1 hippocampus led us to address whether other GABAergic cell types may contribute to the implementation of gamma$_{apical\ tuft}$. Using silicon probes, we recorded unidentified interneurons located in strata radiatum/lacunosum-moleculare. Importantly, somata of PV+ basket cells are not located in these layers but are restricted to strata pyramidale and oriens. Out of 31 putative interneurons recorded in ten experiments from seven animals, we found 12 (39%) that showed enhanced coupling to CSD gamma oscillations in stratum lacunosum-moleculare over other layers. Out of these 12 units, seven neurons showed enhanced coupling to 20–45 Hz CSD oscillations, corresponding to the gamma$_{apical\ tuft}$, and five showed enhanced coupling to fast (60–100 Hz) CSD oscillations (Figures 7C and 7D) ($p < 0.001$ and $p = 0.003$; $F_{8,62} = 9.95$ and $F_{8,44} = 5$; n = 7 and 5 for the two groups, respectively; one-way ANOVA for the coupling strength as a function of input layer). Interestingly, these interneurons fired at various mean theta phases (Figure S4B), suggesting that they represented several distinct cell types. However, all interneurons fired preferentially at or just after the maximum gamma$_{apical\ tuft}$ sink in stratum lacunosum-moleculare (Figures 7E and S4A). This suggests that gamma$_{apical\ tuft}$ is generated by an interplay between gamma-rhythmic excitatory L3 dMEC input in stratum lacunosum-moleculare and local GABAergic interneuron networks.

DISCUSSION

In the CA1 region of the rat hippocampus, at least two distinct gamma oscillations coexist, with opposite theta phase preferences, distinct spatial distributions in CA1 input-layers, and different—yet overlapping—frequency ranges. Similar to a previous report (Colgin et al., 2009), we observed faster gamma oscillations at the trough of theta cycles and independent slower gamma oscillation at the peak and descending phase of theta waves. However, our spatiotemporal CSD analysis disclosed that in both urethane-anaesthetized rats and head-fixed mice the theta-peak gamma oscillations are generated in the distal apical dendritic zone of CA1 (stratum lacunosum-moleculare), where the excitatory innervation from the dMEC terminates (Witter et al., 1988). Together with the selective coupling of putative projection cells in L3 of dMEC, our data suggest that gamma$_{apical\ tuft}$ primarily mediates direct communication between CA1 and dMEC (Charpak et al., 1995). The axons of PV+ basket cells innervate pyramidal cell somata and proximal dendrites selectively in the layers where gamma$_{perisomatic}$ is

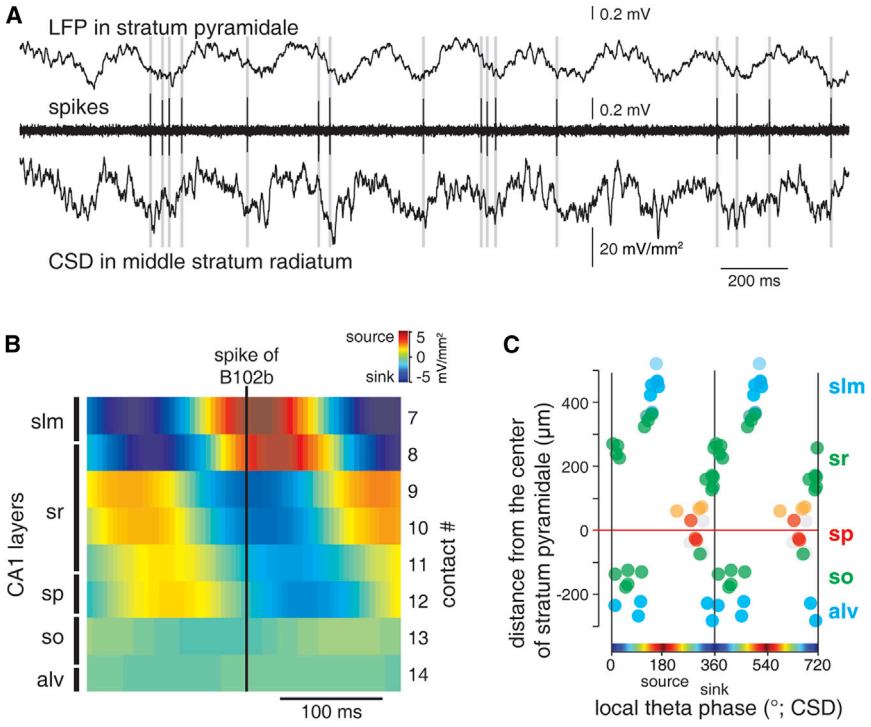

Figure 6. Firing of PV+ Basket Cells Corresponds to Maximal Schaffer Collateral Input during Theta Oscillations

(A) Recordings of spikes from a PV+ basket cell (B102b; middle), LFP from the pyramidal layer (top), and CSD from middle stratum radiatum (bottom). Spikes preferentially occur at the maximum sink (trough) of CSD theta oscillations in stratum radiatum.

(B) Spike-triggered averages of theta-filtered (3–6 Hz) CSDs from silicon probe contacts (right) in different layers (left; same experiment as in [A]; n = 1,283 spikes). Spikes coincide with a sink in middle stratum radiatum.

(C) Mean phase of PV+ basket cell firing (n = 5) relative to CSD theta oscillations recorded at different radial positions (left). Contacts with significant coupling ($\alpha = 0.05$, Rayleigh test) are color coded for layers (right). All cells fire coincident with a sink (at 0° and 360°) in stratum radiatum, approximately 200 µm from stratum pyramidale.

generated, their spikes occur at the same theta phase (Klausberger et al., 2003; Lapray et al., 2012; Varga et al., 2012) as $gamma_{perisomatic}$, and their spike timing is strongly coupled to $gamma_{perisomatic}$ oscillations. This interaction is highly selective, as neither spike timing nor axonal projections of PV+ basket cells contribute to $gamma_{apical\ tuft}$ oscillations. During each theta cycle, when nested $gamma_{perisomatic}$ oscillation is waxing and waning, PV+ basket cells fire with increasing precision on the ascending phase of the CSD gamma cycle, suggesting a cycle-by-cycle buildup of basket cell gamma synchrony, similar to that predicted by some models (Traub et al., 1996; Wang and Buzsáki, 1996; Whittington et al., 1995). This synchrony collapses on the ascending theta phase, when basket cell firing declines and $gamma_{apical\ tuft}$ oscillations replace the $gamma_{perisomatic}$ oscillations. PV+ basket cells in CA1 form a semiautonomous theta-modulated gamma oscillator, influenced by gamma-rhythmic input from CA3 (Csicsvari et al., 2003; Zemankovics et al., 2013) but not by the $gamma_{apical\ tuft}$, which are generated by interactions of glutamatergic input from L3 neurons in dMEC and GABAergic cells, other than PV+ basket cells, situated around the apical tuft. Our data suggest that interneuron types, with their specialized input and output connectivity (Klausberger and Somogyi, 2008), may give rise to distinct subnetworks embedded into the CA1 circuitry, capable of generating, maintaining, and controlling gamma oscillators independently and supporting their integration by CA1 pyramidal cells (Akam and Kullmann, 2010; Colgin et al., 2009). It is important to note that the LFP in the pyramidal cell layer, which has been the most common measure for gamma oscillations, contains a mixture of both gamma oscillations and is even dominated by $gamma_{apical\ tuft}$, which is generated neither in this layer nor by PV+ basket cells.

Role of PV+ Basket Cells in Generating CA1 Gamma Oscillations

The 180° shift in preferred gamma phase of PV+ basket cell firing across the borders of pyramidal layer, together with the coupling strength maintained throughout the perisomatic zone, revealed that rhythmic source-sink fluctuations at ~45 Hz in the pyramidal layer flanked by corresponding sink-source fluctuations in the surrounding dendritic layers constitute the $gamma_{perisomatic}$ oscillation (Csicsvari et al., 2003; Mann et al., 2005). Spikes of PV+ basket cells were followed by the maximum source of gamma-rhythmic CSD oscillations within 3–6 ms in the pyramidal layer, consistent with the $gamma_{perisomatic}$ oscillations being mediated by active, $GABA_A$-receptor-dependent outward currents on pyramidal cell somata, driven by the activation of the basket cell synapses (Bazelot et al., 2010; Glickfeld et al., 2009; Mann et al., 2005; Oren et al., 2010), with oscillations in dendritic layers representing fluctuations associated with passive return currents (Csicsvari et al., 2003; Glickfeld et al., 2009). Indeed, the CA1 circuitry can autonomously generate ~45 Hz oscillations (Middleton et al., 2008; Whittington et al., 1995), whereby the rhythmicity is imposed on the pyramidal cells by an activated network of synaptically interconnected GABAergic cells (Fisahn et al., 2004; Traub et al., 1996; Wang and Buzsáki, 1996; Whittington et al., 1995) or is generated through a loop between inhibitory interneurons and pyramidal cells (Fisahn et al., 1998; Mann et al., 2005). In addition, CA1 interneurons and pyramidal cells can be entrained by the gamma oscillations emerging in the CA3 circuitry, transmitted via the Schaffer collaterals in a pyramidal-interneuron gamma mechanism (Csicsvari et al., 2003; Zemankovics et al., 2013). Schaffer collateral input to PV+ basket cells (together with other inputs; Freund and Antal, 1988) may determine the theta phase modulation of PV+ basket cells (Klausberger et al., 2003; Soltesz and Deschênes, 1993; Ylinen et al., 1995) and, consequently, the phase coupling of

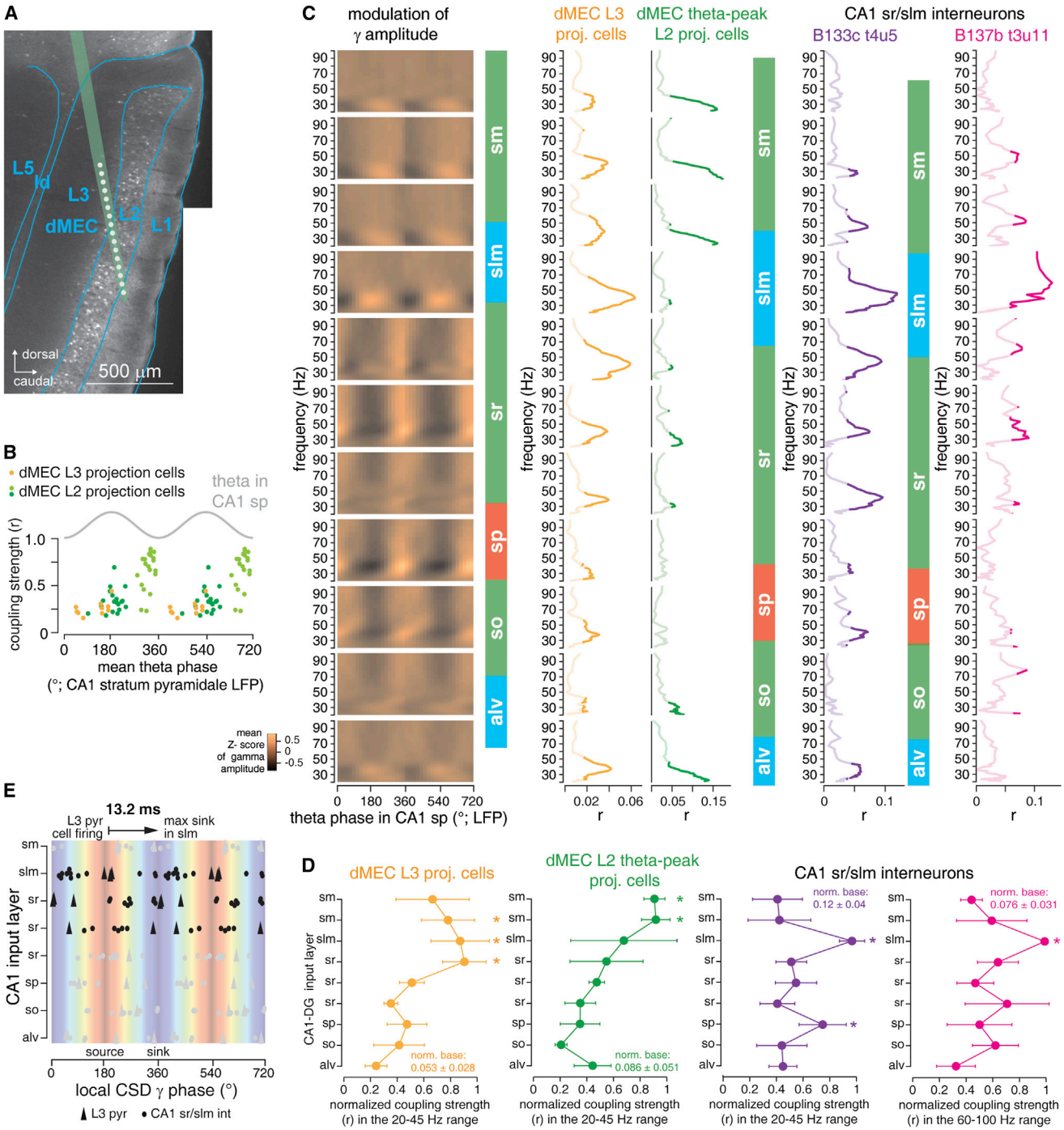

Figure 7. Cellular Organizations of gamma$_{\text{apical tuft}}$

(A) Location of a 16-site silicon probe in dMEC (parasagittal section) shown on an immunofluorescence micrograph with immunolabeling for calbindin for the discrimination of layer boundaries.

(B) Preferred theta-phase versus theta-coupling strength (r) plot of putative projection cells recorded from layer 2 (L2; green) and layer 3 (L3; orange). Only units with significantly nonuniform ($\alpha = 0.05$, Rayleigh test) theta phase distribution are plotted; theta phase was recorded from the CA1 stratum pyramidale. Note that putative L2 projection cells clearly segregate into peak-coupled (dark green) and trough-coupled (light green) units.

(C) First column, CA1 CSD gamma oscillation amplitude as a function of CA1 theta phase and frequency from experiment B136a (857 s cumulative theta duration). Second and third column, phase-coupling strength (r) spectra of L3 putative projection cells (orange), and theta-peak-coupled L2 projection cells (green) to CA1 CSD gamma oscillations. Bright colors indicate significant phase coupling ($\alpha = 0.05$, Rayleigh test). All spikes from putative L3 projection cells (n = 12,672 spikes from 5 units) and theta-peak-coupled L2 projection cells (n = 1,812 spikes from 14 units) were pooled. Note that L3 projection cells couple selectively to CSD

(legend continued on next page)

gamma$_{perisomatic}$ oscillations to theta oscillations (Korotkova et al., 2010).

Gamma Rhythm Specificity of PV+ Basket Cell Output

As discussed above, PV+ basket cells are instrumental for the gamma$_{perisomatic}$ rhythm, but their spike timing and axonal targeting is independent of gamma$_{apical\ tuft}$ oscillations. By minimizing interference, this lack of contribution supports the independence of the two gamma oscillations and is thus consistent with the suggested gamma-rhythm-generator role of CA1 PV+ basket cells. We show that subsets of GABAergic interneurons in strata lacunosum-moleculare and radiatum, as well as putative projection neurons in L3 of the dMEC, contribute selectively to gamma$_{apical\ tuft}$ oscillations. Projection cells in L3 engage in gamma oscillations (Chrobak and Buzsáki, 1998; Colgin et al., 2009; Quilichini et al., 2010), innervate the apical dendritic tufts of CA1 pyramidal cells (Witter et al., 1988), and synaptically drive gamma oscillatory currents in the stratum lacunosum-moleculare (Bragin et al., 1995; Csicsvari et al., 2003) during the peak of the theta cycle (Mizuseki et al., 2009; Quilichini et al., 2010), both in a subset of local GABAergic interneurons and in the apical tufts of CA1 pyramidal cells. Gamma$_{apical\ tuft}$ oscillations are generated by synaptic activity localized in the stratum lacunosum-moleculare, where PV+ basket cells have very sparse dendrites (Gulyás et al., 1999; Tukker et al., 2013), providing a mechanism to minimize direct synaptic entrainment of PV+ basket cells by gamma$_{apical\ tuft}$ and interference in the gamma$_{perisomatic}$ generator circuit.

Interactions between Independent Gamma Oscillations

Long-range synchronization of gamma oscillators between distinct circuits may support associative processes such as sensory binding (Singer, 1999), attention (Gregoriou et al., 2009), and learning (Montgomery and Buzsáki, 2007; Sirota et al., 2008; Tort et al., 2008). In the hippocampus, distinct gamma oscillators may direct information flow for downstream reader networks and may segment theta cycle into functionally different subcycles (Akam and Kullmann, 2010; Buzsáki and Watson, 2012; Colgin et al., 2009). Basket cells control the output timing of CA1 pyramidal cells (Miles et al., 1996), while synaptic excitation and inhibition in distal dendrites may be important for plastic changes in synaptic weights (Lovett-Barron et al., 2012; Miles et al., 1996; Royer et al., 2012). It is therefore tempting to speculate that gamma$_{perisomatic}$ primarily control the transfer of retrieved information to downstream areas and gamma$_{apical\ tuft}$ may control the encoding of novel information. In line with this hypothesis, the first spikes of CA1 pyramidal cells during a place field traversal, when novel associations can be formed (Hasselmo et al., 2002), occur at the peak of theta oscillations (Skaggs et al., 1996), when LTP is facilitated (Hölscher et al., 1997) and gamma$_{apical\ tuft}$ is strong. Due to the theta phase precession of place cell action potentials, established representations of the animal's current location (O'Keefe and Recce, 1993; Skaggs et al., 1996) are expressed on the theta trough when stored information could be efficiently retrieved (Douchamps et al., 2013; Hasselmo et al., 2002) and gamma$_{perisomatic}$ is the dominant fast oscillation. Interestingly, we have observed a significant temporal overlap between these two forms of gamma oscillation during the descending phase of theta oscillation. Although the oscillators are strictly independent, their targets—the CA1 pyramidal cell network—are influenced by both and are in a position to integrate information flows and to form novel associations based on previously established memories. The spike timing of CA1 pyramidal cells, influenced by both gamma oscillators (Colgin et al., 2009), may mediate temporary interaction between the oscillations (Csicsvari et al., 2003). Such temporary coupling may support memory processes (Montgomery and Buzsáki, 2007; Tort et al., 2008). In this scheme, CA1 pyramidal cells are the interface between the two independent gamma oscillations.

Our data suggest that distinct layer-specific gamma oscillators are controlled by specialized GABAergic circuits, which regulate the generation, maintenance, and interaction of such gamma oscillators, supporting the formation of neuronal associations during memory formation and regulating the information flow through distributed neuronal networks.

EXPERIMENTAL PROCEDURES

All animal procedures were performed under licenses approved by the Austrian ministry of Science and in accordance with the relevant regulations of the Medical University of Vienna. Male Sprague-Dawley rats (290–550 g) were anesthetized with urethane (1.25 g/kg body weight) and additional doses of a ketamine/xylazine mixture when necessary (17 and 7 mg/ml, respectively; 0.02–0.1 ml intraperitoneally). To allow combined juxtacellular and silicon probe recordings, two cranial windows were drilled above the dorsal hippocampus, separated by a thin dental cement wall. To improve the mechanical stability necessary for the juxtacellular recordings, after the dura was removed and the electrodes were inserted, the window used to advance the juxtacellular electrode was sealed with wax and the other was kept wet with saline. In other experiments, we have drilled a large cranial

oscillations with a frequency range and spatial distribution corresponding to gamma$_{apical\ tuft}$, while L2 projection cells show selectivity to CSD oscillations recorded in the molecular layer of the dentate gyrus. Fourth and fifth column, coupling strength (r) spectra of two putative interneurons recorded in CA1 strata radiatum/lacunosum-moleculare to CA1 CSD gamma oscillations. Both cells showed increased coupling to CSD gamma oscillations in stratum lacunosum-moleculare but at different gamma frequencies (n = 2,228 and 841 spikes).

(D) Spatial profile of normalized coupling strength (mean vector length, r) of L3 putative projection cells (n = 3 experiments), L2 theta-peak-coupled projection cells (n = 3 experiments), and strata radiatum/lacunosum-moleculare interneurons to CSD gamma oscillations (mean ±SD). Interneurons in strata radiatum/lacunosum-moleculare were included if they showed preferential coupling to either slow (purple; n = 7 cells) or fast (pink; n = 5 cells) CSD gamma oscillations localized to stratum lacunosum-moleculare. Coupling strengths were calculated over frequency ranges as indicated in the plots.

(E) Mean firing phases of L3 pyramidal cells (triangles; n = 3 experiments, spikes pooled) and CA1 stratum radiatum/lacunosum-moleculare interneurons (dots; n = 12 cells) are plotted for all layers relative to local CSD gamma oscillations (calculated for the 20–45 Hz frequency range corresponding to gamma$_{apical\ tuft}$ for L3 pyramidal cells and for the 20–45 Hz or 60–100 Hz frequency range for the interneurons, as appropriate; for clarity, symbols in layers with no gamma$_{apical\ tuft}$ are shown in gray, and overlapping symbols are vertically displaced). The time lag displayed above the plot is calculated assuming a 35 Hz gamma cycle. See also Figure S4.

window above CA3 and CA1 regions and a separate window above the dMEC, when necessary.

Adult C57BL/6 mice (28–31 g) were implanted with a head plate, and a cranial window was drilled above the dorsal CA1 hippocampus under isoflurane-anesthesia. After a recovery period of >2 days, the drug-free mice were fixed to a stereotactic frame via the head plate and were allowed to run on an air-flow-supported Styrofoam ball.

LFP recordings were performed from the dorsal CA1 of anaesthetized rats and head-fixed mice with 16-site linear silicon probes (100 μm and 50 μm intercontact spacing probes in rats and mice, respectively) inserted approximately perpendicular to the layers. In all experiments, the position of the silicon probe was confirmed by post hoc histological analysis, and the individual contacts were aligned to the layers by the recorded activity profiles (ripple oscillations and theta phase reversal). In rats, in parallel, spikes of putative interneurons were recorded by a glass electrode nearby, followed by juxtacellular labeling of the recorded cell for post hoc identification, or unidentified units were recorded by silicon probes nearby in area CA1 stratum radiatum/lacunosum-moleculare, in area CA3, or in the dMEC.

We limited all our analyses of gamma oscillations for periods with theta activity. Theta (3–6 Hz in rats; 5–12 Hz in head-fixed mice) phase at any time point was determined by linear extrapolation between trough (0°) and the forthcoming peak (180°), or between the peak and the forthcoming trough (360°), and is reported from the contact in stratum pyramidale or equivalent, unless stated otherwise.

Under the assumption that CSD sink-source pairs have radial orientation, CSD at a given contact was estimated as the second spatial derivative of the LFP in the axis of the silicon probe before any further transformations (filtering, wavelet) were applied. Instantaneous amplitude and phase of gamma oscillation was extracted by a continuous complex Morlet wavelet transformation (wavelet parameters of 1 and 1.5; 40 and 52 logarithmically equidistant scales between 20–100 Hz and 20–150 Hz for anesthetized and drug-free animals, respectively; filtering was performed only for visual inspection and display). For all CSD data, 0° and 360° represent the maximum sink and 180° represent the maximum source. For calculating the theta-gamma cross-frequency phase-amplitude coupling, we summed the Z-scored, theta-binned wavelet amplitudes for each scale, across the whole theta period in that experiment. Spike phase coupling statistics were calculated on matrices generated by spike-triggered extraction of complex wavelet values.

SUPPLEMENTAL INFORMATION

Supplemental Information includes four figures and Supplemental Experimental Procedures and can be found with this article online at http://dx.doi.org/10.1016/j.neuron.2014.01.021.

ACKNOWLEDGMENTS

The authors thank Romana Hauer for the reconstruction of the cell B96b and Romana Hauer and Erzsébet Borók for the excellent technical assistance. We thank Hugo Malagon-Vina for expert contributions to unit clustering, Thomas Forro for help with the head-fixed mice recordings, Peter Somogyi and Norbert Hájos for commenting on an earlier version of this manuscript, and members of the Klausberger and Somogyi labs for discussions on the data. This work was supported in part by grant 242689 of the European Research Council and grant SCIC03 of the Vienna Science and Technology Fund.

Accepted: December 18, 2013
Published: March 5, 2014

REFERENCES

Akam, T., and Kullmann, D.M. (2010). Oscillations and filtering networks support flexible routing of information. Neuron *67*, 308–320.

Bazelot, M., Dinocourt, C., Cohen, I., and Miles, R. (2010). Unitary inhibitory field potentials in the CA3 region of rat hippocampus. J. Physiol. *588*, 2077–2090.

Belluscio, M.A., Mizuseki, K., Schmidt, R., Kempter, R., and Buzsáki, G. (2012). Cross-frequency phase-phase coupling between θ and γ oscillations in the hippocampus. J. Neurosci. *32*, 423–435.

Bragin, A., Jandó, G., Nádasdy, Z., Hetke, J., Wise, K., and Buzsáki, G. (1995). Gamma (40-100 Hz) oscillation in the hippocampus of the behaving rat. J. Neurosci. *15*, 47–60.

Buzsáki, G., and Draguhn, A. (2004). Neuronal oscillations in cortical networks. Science *304*, 1926–1929.

Buzsáki, G., and Watson, B.O. (2012). Brain rhythms and neural syntax: implications for efficient coding of cognitive content and neuropsychiatric disease. Dialogues Clin. Neurosci. *14*, 345–367.

Buzsáki, G., Anastassiou, C.A., and Koch, C. (2012). The origin of extracellular fields and currents—EEG, ECoG, LFP and spikes. Nat. Rev. Neurosci. *13*, 407–420.

Canolty, R.T., Edwards, E., Dalal, S.S., Soltani, M., Nagarajan, S.S., Kirsch, H.E., Berger, M.S., Barbaro, N.M., and Knight, R.T. (2006). High gamma power is phase-locked to theta oscillations in human neocortex. Science *313*, 1626–1628.

Cardin, J.A., Carlén, M., Meletis, K., Knoblich, U., Zhang, F., Deisseroth, K., Tsai, L.H., and Moore, C.I. (2009). Driving fast-spiking cells induces gamma rhythm and controls sensory responses. Nature *459*, 663–667.

Charpak, S., Paré, D., and Llinás, R. (1995). The entorhinal cortex entrains fast CA1 hippocampal oscillations in the anaesthetized guinea-pig: role of the monosynaptic component of the perforant path. Eur. J. Neurosci. *7*, 1548–1557.

Chrobak, J.J., and Buzsáki, G. (1998). Gamma oscillations in the entorhinal cortex of the freely behaving rat. J. Neurosci. *18*, 388–398.

Colgin, L.L., and Moser, E.I. (2010). Gamma oscillations in the hippocampus. Physiology (Bethesda) *25*, 319–329.

Colgin, L.L., Denninger, T., Fyhn, M., Hafting, T., Bonnevie, T., Jensen, O., Moser, M.B., and Moser, E.I. (2009). Frequency of gamma oscillations routes flow of information in the hippocampus. Nature *462*, 353–357.

Csicsvari, J., Jamieson, B., Wise, K.D., and Buzsáki, G. (2003). Mechanisms of gamma oscillations in the hippocampus of the behaving rat. Neuron *37*, 311–322.

Douchamps, V., Jeewajee, A., Blundell, P., Burgess, N., and Lever, C. (2013). Evidence for encoding versus retrieval scheduling in the hippocampus by theta phase and acetylcholine. J. Neurosci. *33*, 8689–8704.

Fernández-Ruiz, A., Makarov, V.A., Benito, N., and Herreras, O. (2012). Schaffer-specific local field potentials reflect discrete excitatory events at gamma frequency that may fire postsynaptic hippocampal CA1 units. J. Neurosci. *32*, 5165–5176.

Fisahn, A., Pike, F.G., Buhl, E.H., and Paulsen, O. (1998). Cholinergic induction of network oscillations at 40 Hz in the hippocampus in vitro. Nature *394*, 186–189.

Fisahn, A., Contractor, A., Traub, R.D., Buhl, E.H., Heinemann, S.F., and McBain, C.J. (2004). Distinct roles for the kainate receptor subunits GluR5 and GluR6 in kainate-induced hippocampal gamma oscillations. J. Neurosci. *24*, 9658–9668.

Freund, T.F., and Antal, M. (1988). GABA-containing neurons in the septum control inhibitory interneurons in the hippocampus. Nature *336*, 170–173.

Glickfeld, L.L., Roberts, J.D., Somogyi, P., and Scanziani, M. (2009). Interneurons hyperpolarize pyramidal cells along their entire somatodendritic axis. Nat. Neurosci. *12*, 21–23.

Gregoriou, G.G., Gotts, S.J., Zhou, H., and Desimone, R. (2009). High-frequency, long-range coupling between prefrontal and visual cortex during attention. Science *324*, 1207–1210.

Gulyás, A.I., Megías, M., Emri, Z., and Freund, T.F. (1999). Total number and ratio of excitatory and inhibitory synapses converging onto single interneurons

of different types in the CA1 area of the rat hippocampus. J. Neurosci. *19*, 10082–10097.

Gulyás, A.I., Szabó, G.G., Ulbert, I., Holderith, N., Monyer, H., Erdélyi, F., Szabó, G., Freund, T.F., and Hájos, N. (2010). Parvalbumin-containing fast-spiking basket cells generate the field potential oscillations induced by cholinergic receptor activation in the hippocampus. J. Neurosci. *30*, 15134–15145.

Hasselmo, M.E., Bodelón, C., and Wyble, B.P. (2002). A proposed function for hippocampal theta rhythm: separate phases of encoding and retrieval enhance reversal of prior learning. Neural Comput. *14*, 793–817.

Hölscher, C., Anwyl, R., and Rowan, M.J. (1997). Stimulation on the positive phase of hippocampal theta rhythm induces long-term potentiation that can be depotentiated by stimulation on the negative phase in area CA1 in vivo. J. Neurosci. *17*, 6470–6477.

Jackson, J., Goutagny, R., and Williams, S. (2011). Fast and slow γ rhythms are intrinsically and independently generated in the subiculum. J. Neurosci. *31*, 12104–12117.

Kajikawa, Y., and Schroeder, C.E. (2011). How local is the local field potential? Neuron *72*, 847–858.

Klausberger, T., and Somogyi, P. (2008). Neuronal diversity and temporal dynamics: the unity of hippocampal circuit operations. Science *321*, 53–57.

Klausberger, T., Magill, P.J., Márton, L.F., Roberts, J.D., Cobden, P.M., Buzsáki, G., and Somogyi, P. (2003). Brain-state- and cell-type-specific firing of hippocampal interneurons in vivo. Nature *421*, 844–848.

Korotkova, T., Fuchs, E.C., Ponomarenko, A., von Engelhardt, J., and Monyer, H. (2010). NMDA receptor ablation on parvalbumin-positive interneurons impairs hippocampal synchrony, spatial representations, and working memory. Neuron *68*, 557–569.

Lapray, D., Lasztoczi, B., Lagler, M., Viney, T.J., Katona, L., Valenti, O., Hartwich, K., Borhegyi, Z., Somogyi, P., and Klausberger, T. (2012). Behavior-dependent specialization of identified hippocampal interneurons. Nat. Neurosci. *15*, 1265–1271.

Lasztóczi, B., Tukker, J.J., Somogyi, P., and Klausberger, T. (2011). Terminal field and firing selectivity of cholecystokinin-expressing interneurons in the hippocampal CA3 area. J. Neurosci. *31*, 18073–18093.

Lisman, J.E., and Idiart, M.A.P. (1995). Storage of 7 +/- 2 short-term memories in oscillatory subcycles. Science *267*, 1512–1515.

Lisman, J.E., and Jensen, O. (2013). The θ-γ neural code. Neuron *77*, 1002–1016.

Lovett-Barron, M., Turi, G.F., Kaifosh, P., Lee, P.H., Bolze, F., Sun, X.H., Nicoud, J.F., Zemelman, B.V., Sternson, S.M., and Losonczy, A. (2012). Regulation of neuronal input transformations by tunable dendritic inhibition. Nat. Neurosci. *15*, 423–430, S1–S3.

Mann, E.O., and Mody, I. (2010). Control of hippocampal gamma oscillation frequency by tonic inhibition and excitation of interneurons. Nat. Neurosci. *13*, 205–212.

Mann, E.O., Suckling, J.M., Hajos, N., Greenfield, S.A., and Paulsen, O. (2005). Perisomatic feedback inhibition underlies cholinergically induced fast network oscillations in the rat hippocampus in vitro. Neuron *45*, 105–117.

Middleton, S., Jalics, J., Kispersky, T., Lebeau, F.E., Roopun, A.K., Kopell, N.J., Whittington, M.A., and Cunningham, M.O. (2008). NMDA receptor-dependent switching between different gamma rhythm-generating microcircuits in entorhinal cortex. Proc. Natl. Acad. Sci. USA *105*, 18572–18577.

Miles, R., Tóth, K., Gulyás, A.I., Hájos, N., and Freund, T.F. (1996). Differences between somatic and dendritic inhibition in the hippocampus. Neuron *16*, 815–823.

Mizuseki, K., Sirota, A., Pastalkova, E., and Buzsáki, G. (2009). Theta oscillations provide temporal windows for local circuit computation in the entorhinal-hippocampal loop. Neuron *64*, 267–280.

Montgomery, S.M., and Buzsáki, G. (2007). Gamma oscillations dynamically couple hippocampal CA3 and CA1 regions during memory task performance. Proc. Natl. Acad. Sci. USA *104*, 14495–14500.

O'Keefe, J., and Recce, M.L. (1993). Phase relationship between hippocampal place units and the EEG theta rhythm. Hippocampus *3*, 317–330.

Oren, I., Hájos, N., and Paulsen, O. (2010). Identification of the current generator underlying cholinergically induced gamma frequency field potential oscillations in the hippocampal CA3 region. J. Physiol. *588*, 785–797.

Quilichini, P., Sirota, A., and Buzsáki, G. (2010). Intrinsic circuit organization and theta-gamma oscillation dynamics in the entorhinal cortex of the rat. J. Neurosci. *30*, 11128–11142.

Ray, S., and Maunsell, J.H. (2010). Differences in gamma frequencies across visual cortex restrict their possible use in computation. Neuron *67*, 885–896.

Royer, S., Zemelman, B.V., Losonczy, A., Kim, J., Chance, F., Magee, J.C., and Buzsáki, G. (2012). Control of timing, rate and bursts of hippocampal place cells by dendritic and somatic inhibition. Nat. Neurosci. *15*, 769–775.

Scheffer-Teixeira, R., Belchior, H., Caixeta, F.V., Souza, B.C., Ribeiro, S., and Tort, A.B. (2012). Theta phase modulates multiple layer-specific oscillations in the CA1 region. Cereb. Cortex *22*, 2404–2414.

Singer, W. (1999). Neuronal synchrony: a versatile code for the definition of relations? Neuron *24*, 49–65, 111–125.

Sirota, A., Montgomery, S., Fujisawa, S., Isomura, Y., Zugaro, M., and Buzsáki, G. (2008). Entrainment of neocortical neurons and gamma oscillations by the hippocampal theta rhythm. Neuron *60*, 683–697.

Skaggs, W.E., McNaughton, B.L., Wilson, M.A., and Barnes, C.A. (1996). Theta phase precession in hippocampal neuronal populations and the compression of temporal sequences. Hippocampus *6*, 149–172.

Soltesz, I., and Deschênes, M. (1993). Low- and high-frequency membrane potential oscillations during theta activity in CA1 and CA3 pyramidal neurons of the rat hippocampus under ketamine-xylazine anesthesia. J. Neurophysiol. *70*, 97–116.

Stumpf, C. (1965). The fast component in the electrical activity of rabbit's hippocampus. Electroencephalogr. Clin. Neurophysiol. *18*, 477–486.

Tort, A.B., Kramer, M.A., Thorn, C., Gibson, D.J., Kubota, Y., Graybiel, A.M., and Kopell, N.J. (2008). Dynamic cross-frequency couplings of local field potential oscillations in rat striatum and hippocampus during performance of a T-maze task. Proc. Natl. Acad. Sci. USA *105*, 20517–20522.

Tort, A.B., Komorowski, R.W., Manns, J.R., Kopell, N.J., and Eichenbaum, H. (2009). Theta-gamma coupling increases during the learning of item-context associations. Proc. Natl. Acad. Sci. USA *106*, 20942–20947.

Townsend, G., Peloquin, P., Kloosterman, F., Hetke, J.F., and Leung, L.S. (2002). Recording and marking with silicon multichannel electrodes. Brain Res. Brain Res. Protoc. *9*, 122–129.

Traub, R.D., Whittington, M.A., Colling, S.B., Buzsáki, G., and Jefferys, J.G. (1996). Analysis of gamma rhythms in the rat hippocampus in vitro and in vivo. J. Physiol. *493*, 471–484.

Tukker, J.J., Fuentealba, P., Hartwich, K., Somogyi, P., and Klausberger, T. (2007). Cell type-specific tuning of hippocampal interneuron firing during gamma oscillations in vivo. J. Neurosci. *27*, 8184–8189.

Tukker, J.J., Lasztóczi, B., Katona, L., Roberts, J.D., Pissadaki, E.K., Dalezios, Y., Márton, L., Zhang, L., Klausberger, T., and Somogyi, P. (2013). Distinct dendritic arborization and in vivo firing patterns of parvalbumin-expressing basket cells in the hippocampal area CA3. J. Neurosci. *33*, 6809–6825.

Varga, C., Golshani, P., and Soltesz, I. (2012). Frequency-invariant temporal ordering of interneuronal discharges during hippocampal oscillations in awake mice. Proc. Natl. Acad. Sci. USA *109*, E2726–E2734.

Wang, X.J., and Buzsáki, G. (1996). Gamma oscillation by synaptic inhibition in a hippocampal interneuronal network model. J. Neurosci. *16*, 6402–6413.

Whittington, M.A., Traub, R.D., and Jefferys, J.G.R. (1995). Synchronized oscillations in interneuron networks driven by metabotropic glutamate receptor activation. Nature *373*, 612–615.

Witter, M.P., Griffioen, A.W., Jorritsma-Byham, B., and Krijnen, J.L.M. (1988). Entorhinal projections to the hippocampal CA1 region in the rat: an underestimated pathway. Neurosci. Lett. *85*, 193–198.

Ylinen, A., Soltész, I., Bragin, A., Penttonen, M., Sik, A., and Buzsáki, G. (1995). Intracellular correlates of hippocampal theta rhythm in identified pyramidal cells, granule cells, and basket cells. Hippocampus *5*, 78–90.

Zemankovics, R., Veres, J.M., Oren, I., and Hájos, N. (2013). Feedforward inhibition underlies the propagation of cholinergically induced gamma oscillations from hippocampal CA3 to CA1. J. Neurosci. *33*, 12337–12351.

Neuron, Volume *81*

Supplemental Information

Layer-Specific GABAergic Control of Distinct Gamma Oscillations in the CA1 Hippocampus

Bálint Lasztóczi and Thomas Klausberger

SUPPLEMETARY FIGURES

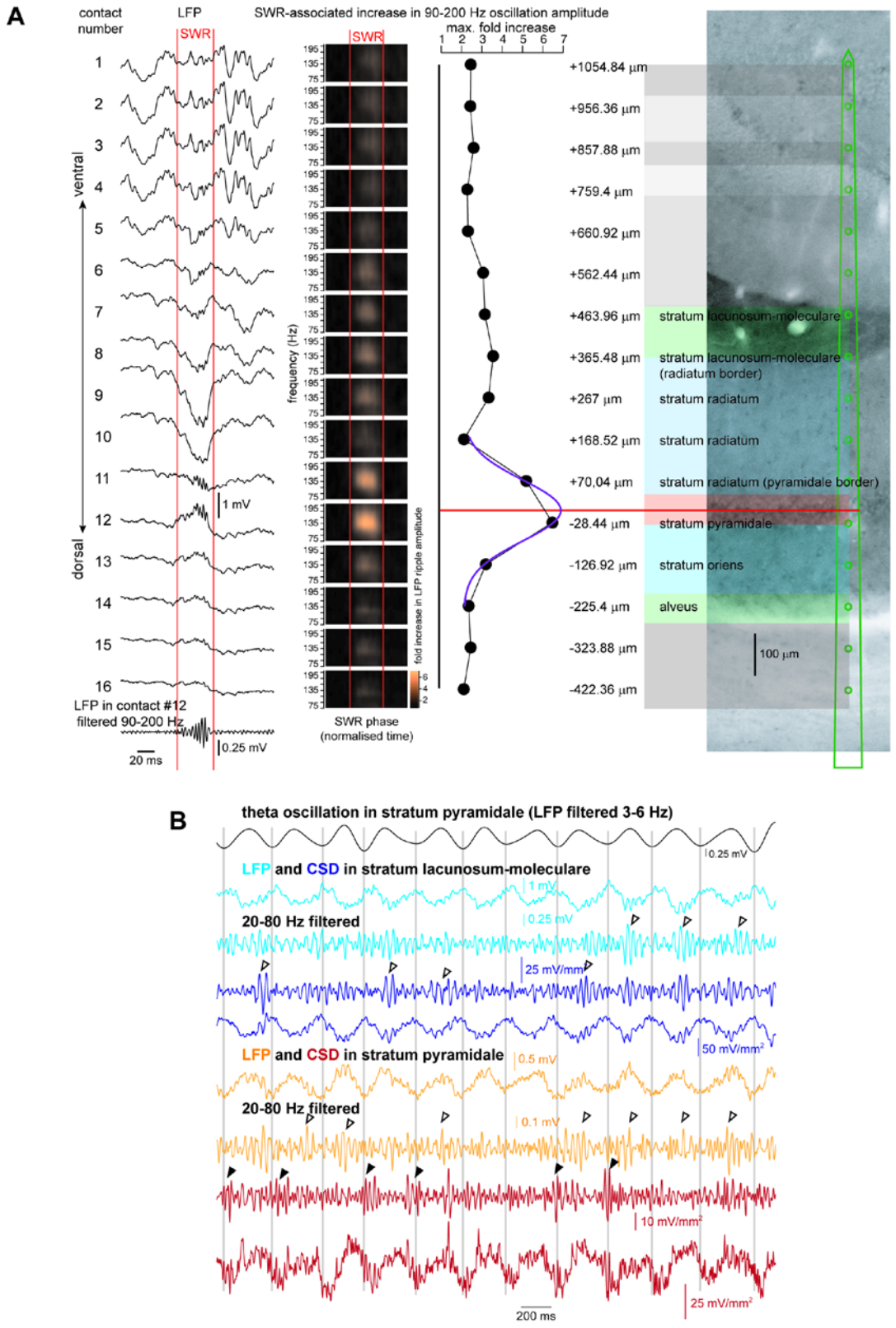

Supplementary Figure 1 (associated to Figure 1). (A) Alignment of silicon probe contacts to layers of the hippocampus. Local field potential recordings (left) during a representative sharp-wave ripple

(SWR) event from the 16 individual contact sites of a silicon probe (16 sites arranged linearly on a single shank with 100 µm spacing; 10° rostral-to-caudal angle) inserted into the CA1 area of the dorsal hippocampus piercing roughly perpendicularly across the anatomical layers (experiment B102). Channels are numbered from the most ventral (top; #1) to the most dorsal (bottom; #16). Red lines mark the start and the end of SWR. We observed 1 or 2 contacts with strong 90 - 200 Hz oscillations (ripple; see the filtered trace in the bottom), signaling the approximate depth of stratum pyramidale. In line with reported activity profiles, 0 - 100 µm ventral from these contacts, in proximal stratum radiatum sharp-waves reversed from positive- to negative-going (Ylinen et al., 1995a; traces on the left, compare contact #13 and contacts #10, 9 and 8), and ~200 µm ventral from these contacts (in middle stratum radiatum) theta oscillations also phase-reversed (Ylinen et al., 1995b; not shown), which approximately identified the distribution of contacts in CA1 layers during the experiment. Second column shows time normalized time-frequency-LFP amplitude plots from wavelet transforms (75-200 Hz, 50 logarithmically equidistant coefficients) averaged across SWRs (n = 79), and normalized to the pre-SWR level for each frequency (color-coded plots; red lines indicate the start and the end of SWRs). The maxima plotted as a function of contact number are shown as a depth profile in the middle (due to the 10° angle, inter-contact spacing of 98.48 µm was used for calculations). The centre of the Gaussian (purple trace) fitted to the perisomatic zone of this profile (contacts #10-14), identifies the middle of stratum pyramidale (Mizuseki et al., 2011; horizontal red line taken as origin) and defines the contact locations (negative and positive numbers representing dorsal and ventral directions, respectively). We analyzed the electrode location also with histological methods, and observed an elongated, restricted tissue lesions of dorso-ventral orientation, which we identified as the track of the silicon probe (right). Tracks spanned several 70 µm thick sections through the neocortex and CA1, and penetrated the dentate gyrus. In one of the sections the layer boundaries were recorded at the medio-lateral position of the electrode track (right: epifluorescent photomicrograph taken with a 4x magnification objective scaled and aligned to the silicon probe recording positions; streptavidin-Alexa488 background labeling). The contacts were then aligned to the centre of the pyramidal layer and their location was recorded with respect to anatomical layers. In one experiment (B96b), the alignment was confirmed by 3D reconstruction (B96b; Figure 2B). **B; CSD and LFP gamma oscillations in stratum pyramidale and stratum lacunosum-moleculare.** Representative LFP and CSD recordings from the stratum pyramidale and stratum lacunosum-moleculare. Unfiltered traces as well as traces band-pass filtered for gamma oscillations (20 – 80 Hz) are shown. The open and filled arrowheads mark $\text{gamma}_{\text{apical tuft}}$ and $\text{gamma}_{\text{perisomatic}}$ oscillations. The vertical grey lines mark theta troughs recorded from LFP in stratum pyramidale.

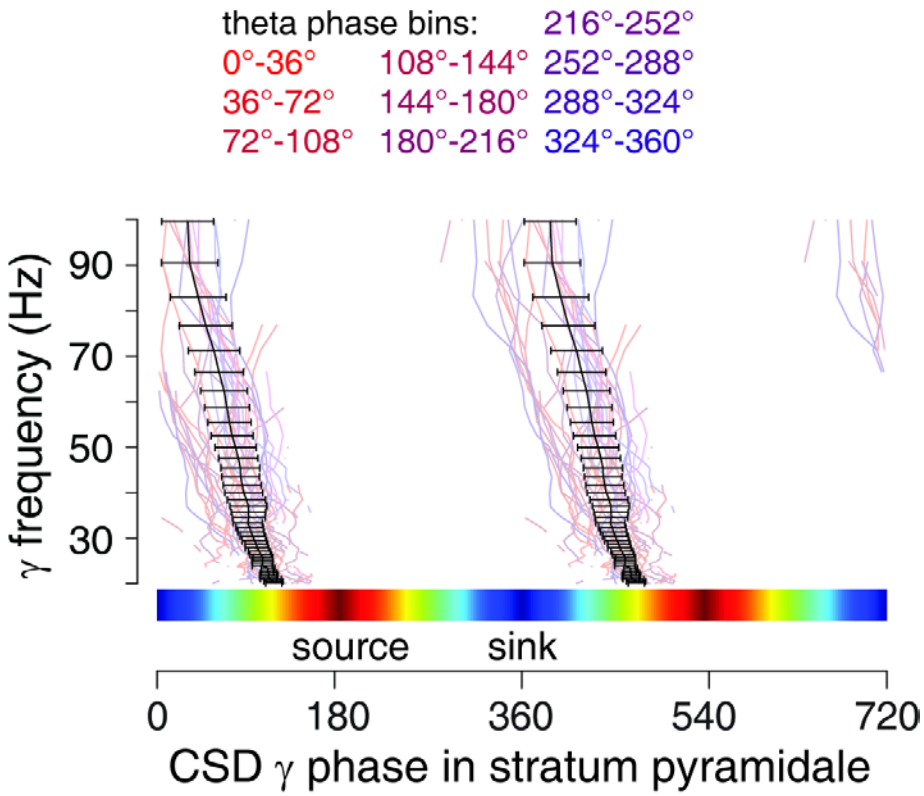

Supplementary Figure 2 (associated to Figure 4). The preferred gamma$_{perisomatic}$ phase of PV+ basket cells does not change as a function of theta phase. Mean phase spectrum of PV+ basket cell firing relative to CSD oscillations in stratum pyramidale (black, circular mean ± circular SD; n = 5). Mean phase spectra during different phases of theta cycle are displayed color-coded (theta phase bins as in Figure 4; only significant values are plotted for each cell; α = 0.05, Rayleigh test). No systematic variations in preferred gamma phase are observed for the different theta phase bins. Note that the preferred phase shows a marked forward shift with decreasing frequency over the whole gamma-range.

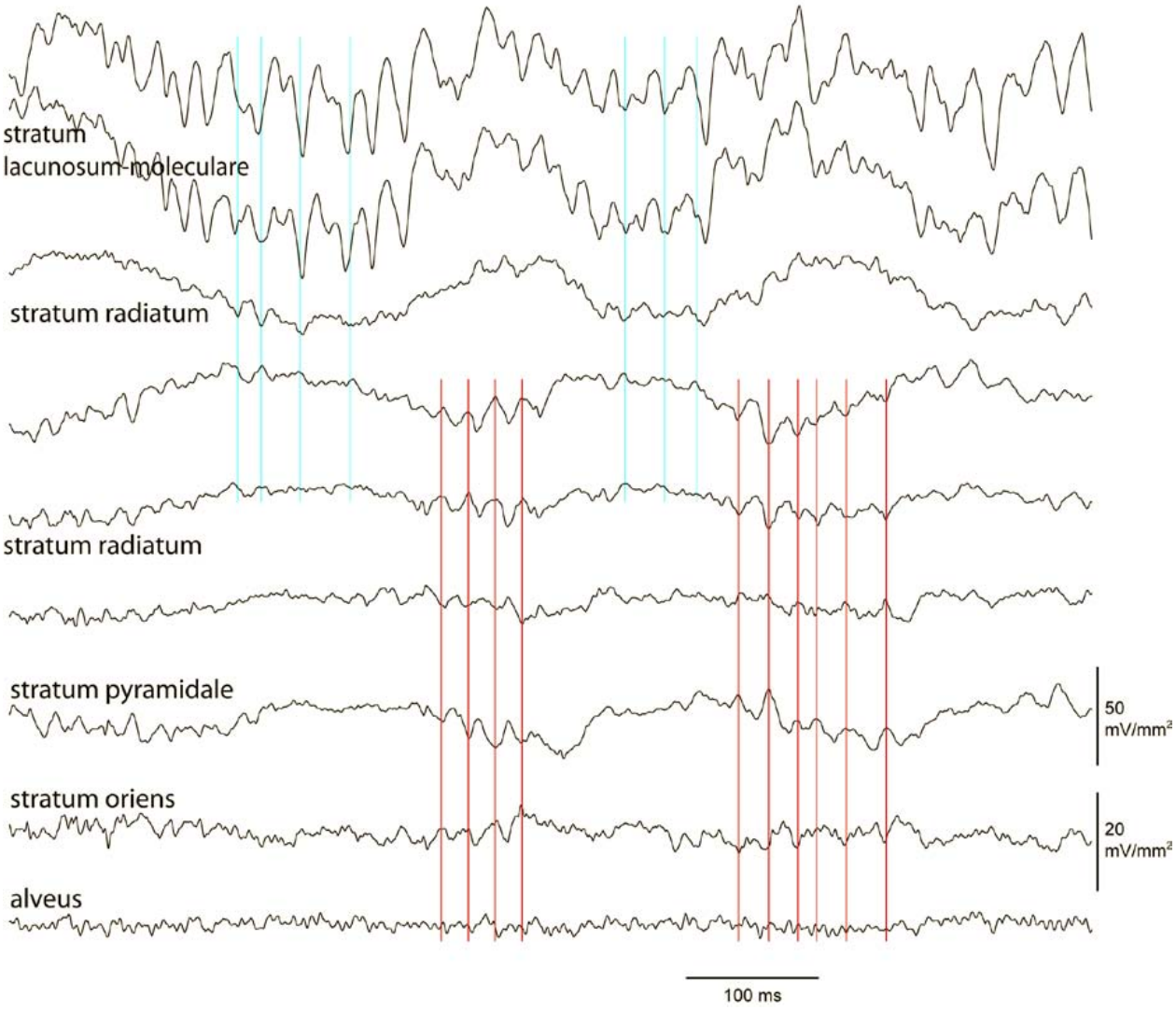

Supplementary Figure 3 (associated to Figure 5). CSD sink-source pairs across the radial axis of the CA1. CSD recordings (smoothed with a 1 ms time constant) from the contacts located in different layers across the radial axis of the hippocampal CA1 region. The same 9 contacts are displayed as in Figure 2 (from experiment B96b). The gamma oscillatory source-sink alternation in the stratum pyramidale (contacts 3 and 4 from the bottom) has its respective inverted oscillatory activity (sink-source alternation) in strata oriens and radiatum (contacts 2 and 5-6 from the bottom, respectively). This arrangement represents an oscillatory tripole centered on the stratum pyramidale, with discernible active and passive components (which we term $gamma_{perisomatic}$). Individual oscillatory cycles are highlighted by vertical red lines. Similarly, many oscillatory cycles in stratum lacunosum-moleculare (2_{nd} contact from the top) have their respective inverted counterparts in stratum radiatum (4_{th} contact from the top). This arrangement represents an oscillatory dipole phase-reversing at the border between strata lacunosum-moleculare and radiatum ($gamma_{apical\ tuft}$; cf. Figure 7E and S4). Note that CSD in stratum radiatum represents a mixture of different oscillations. Note the different amplitude scales for the bottom 2 traces and the top 7 traces.

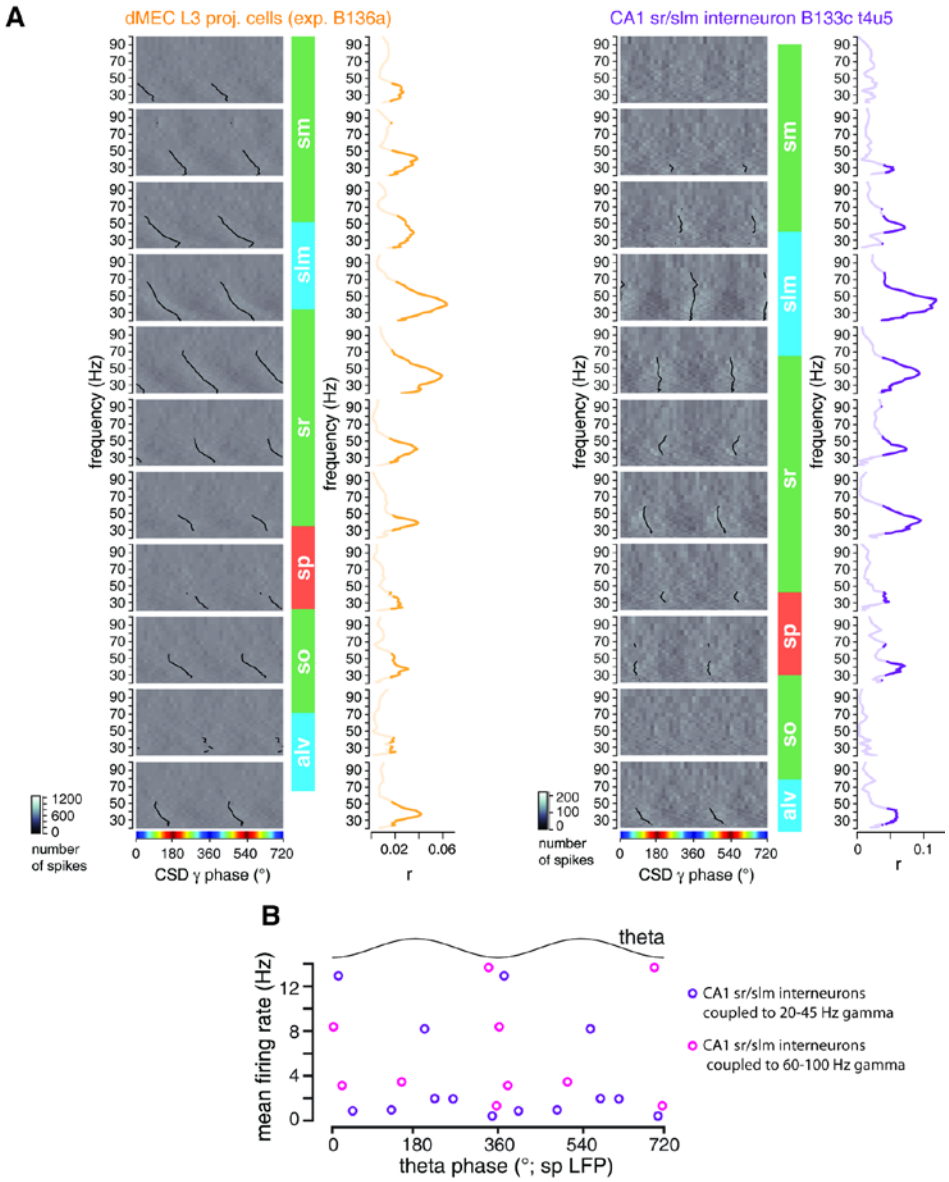

Supplementary Figure 4 (associated to Figure 7) Spike timing of L3 dMEC putative projection neurons and CA1 stratum radiatum/lacunosum-moleculare interneurons. (A) Coupling of spike timing to CSD gamma oscillations in different layers. Data from a L3 dMEC recording (left; same as in Figure 7C) and from one stratum radiatum/lacunosum-moleculare interneuron phase-coupled to $gamma_{apical\ tuft}$ (right; same as in Figure 7C) are shown. Left; spike density plots (color-coded spike count as a function of CSD oscillation phase for each frequency; two cycles are shown, maximum sink is 0° and 360° and maximum source is 180°), and mean firing phase spectra (black lines, only significant values plotted; Rayleigh test, $\alpha = 0.05$); The coupling strength spectra and the input-layer borders are re-plotted from Figure 7C, for comparison. **(B)** Spike timing of CA1 stratum radiatum/lacunosum-moleculare interneurons phase coupled to 20-45 Hz (purple; $gamma_{apical\ tuft}$) or 60-100 Hz (pink) CSD gamma oscillations in the stratum lacunosum-moleculare. The firing rate during theta oscillations is plotted as a function of the mean firing phase. Note the scattering of the data points for both groups.

SUPPLEMENTAL EXPERIMENTAL PROCEDURES

Electrophysiological recordings

Spikes of putative interneurons were recorded (filtered 0.8 - 5 kHz; sampled at 20 kHz) in the dorsal CA1 hippocampus with an extracellular glass electrode (10° posterior-anterior angle, 4 - 4.2 mm posterior, 2 - 2.3 mm right from Bregma) filled with 3% neurobiotin in 0.5 M NaCl. Subsequently, the recorded cell was labeled with neurobiotin using the juxtacellular method (Pinault, 1996). In rats, LFP (filtered 0.1 - 475 Hz, sampled at 2 kHz) was recorded with a linear silicon probe (single shank, 16 sites with 100 µm spacing, 703 μm^2 area, Neuronexus) connected to Lynx-8 amplifiers (Neuralynx) through an RA16-AC preamplifier (Tucker-Davies), inserted in a 10° anterior-posterior angle, 2.8 - 3 mm posterior and 1.9 - 2 mm right from Bregma, tip ~3.3 mm from the brain surface. In some experiments where additional Silicon Probes were inserted to record unit activity a right angle or a medial-lateral 10° angle was used. In head-fixed mice recordings were made wide-band (0.1 - 6000 Hz; 20 kHz sampling rate), and were subsequently filtered (800 Hz low-pass filter) and down-sampled (to 2 kHz) digitally.

To record units from the dMEC and CA3 or CA1 area we inserted an additional linear single shank, 16 sites silicon probe with 50 µm spacing, (703 μm^2 area, Neuronexus; connected to a RA16-AC preamplifier, Tucker-Davies), or a 4 shank silicon probe (150 µm inter-shank distance; tetrode arrangement of 4 contacts per shank; Neuronexus) and recorded the wide-band (0.1 - 6000 Hz) electrophysiological signal at 20 kHz sampling rate (Csicsvari et al., 2003). Electrodes targeting dMEC were inserted at 4.5 mm right and 8.8 mm caudal from the bregma at a 10° anterior-posterior angle (tip depth; 3.4 - 4.8 mm); the position of the border between layer 2 and layer 1 of dMEC was identified based on the theta phase reversal (Mizuseki et al., 2009; Quilichini et al., 2010). Electrodes targeting CA3 were inserted 4 - 4.5 mm right and 3.5 mm caudal from Bregma at a 10° lateral-medial angle (tip depth: 3.5 - 4.1 mm). Electrodes targeting CA1 were inserted at 2.4-2.8 mm right and 3.1- 3.5 mm caudal from the Bregma with a 0 or 10° lateral-medial angle. The location of the recorded unit in CA1 was inferred from comparing the recorded wide-band signal to the LFP signals from the other silicon-probe. Detailed description of the recording system, further details of recording procedures, and clustering of single units have been reported earlier (Lasztoczi et al., 2011; Tukker et al., 2013).

Recordings from head-fixed mice

C57BL/6 mice were implanted with a head-plate and fixed to the stereotactic apparatus while running on a styrofoam ball supported by constant air flow. At the time of the head-plate implantation a cranial window was drilled above the dorsal hippocampus (1 mm right and 1.8 mm caudal from the Bregma). Several days later a 16-site silicon-probe (contacts arranged linearly on a single shank with 50 µm spacing), was inserted through the cranial window and the LFP was recorded across the input layers of the CA1 (see above).

Analysis of theta and gamma oscillations

Theta oscillation periods were identified in down-sampled (200 Hz) and filtered (3 – 6 Hz and 5 - 12 Hz band-pass FIR filter, for the anaesthetized and head-fixed animals, respectively) LFP or CSD

signal. Unless indicated otherwise, LFP theta oscillation was used from stratum pyramidale or oriens as a reference.

Amplitude and phase of gamma oscillation was extracted by using a wavelet-based approach (filtering was performed only for visual inspection and display). Periods of theta oscillation (extended at the beginning and at the end to avoid edge effects; CSD and LFP) were subjected to continuous wavelet transformation between 20 and 100 Hz with scales for 40 logarithmically equidistant frequencies, with a complex Morlet wavelet (wavelet parameters of 1 and 1.5; for the head fixed mice gamma oscillations were analyzed between 20 - 150 Hz, with scales for 52 logarithmically equidistant frequencies). When analyzing amplitude modulation of gamma oscillations by theta, we first Z-scored the wavelet amplitudes (absolute values of the complex vector) for each frequency separately across the whole period included. Each theta cycle was divided into 20 equal length bins, and the mean of the Z-scored amplitude was calculated within each bin, followed by averaging across theta cycles. To analyze phase coupling of the cells, at the time of each detected spike the instantaneous phase spectra were extracted (angles of the complex wavelet, 0° is maximum sink, or trough, and 180° is maximum source, or peak) and collected in a matrix, from which we calculated spike-phase distributions (phase histograms with 18° bins), mean phase angles, mean vector lengths, and circular statistics (Rayleigh test) to assess significance (at α = 0.05), for each frequency (scale) separately. Results of these analyses are presented in a spectral form.

To determine the frequency span occupied by $gamma_{perisomatic}$ and $gamma_{apical\ tuft}$ oscillations, we detected peaks of the amplitude modulation index spectra (difference between the within-theta-cycle maxima and minima of the mean amplitude Z-score for each frequency), and determined the frequency at which this occurred (centre frequency). The frequency ranges were then defined by expansion towards higher and lower frequencies until the values decreased below 75% of the peak. $Gamma_{perisomatic}$ ranges were determined in stratum pyramidale (except experiment B117a; stratum oriens) and $gamma_{apical\ tuft}$ ranges were determined from stratum lacunosum-moleculare.

To calculate the theta phase dependent modulation of gamma phase coupling, we divided each theta cycle into 10 equal length bins. As the statistics depend on the number of observations, to account for unequal sample numbers that results from the theta modulation of the firing rate, we took a random sample of $n = \min(n_{bin1}, n_{bin2},..., n_{bin10})$ spikes from each bin. Gamma coupling statistics were calculated for each sample as described above.

Spatial profiles of different parameters are presented either as a function of distance from the middle of stratum pyramidale (theta) or for contacts in different layers (gamma phase). In the latter case, locations at the border of two layers were omitted.

Current-source-density-analysis and electrode placement

To preserve all oscillatory components we calculated CSDs for each silicon probe contact on a sample-by-sample basis before any further processing. In laminated structures, CSD is related to the second spatial derivative of the LFP by the equation

$$-I_m = \sigma_z \cdot \frac{\partial^2 \phi}{\partial z^2}$$

where I_m is the CSD, ϕ is the potential (LFP), z is the direction perpendicular to the laminae, and σ_z is the z-directional component of the tissue conductivity tensor (Mitzdorf, 1985). As we were primarily interested in temporal dynamics and relative amplitude of CSD, and σ_z is not easily accessible experimentally, we estimated the unscaled CSD at silicon probe contact n, and time t ($CSD_{n,t}$) by

$$CSD_{n,t} = -\frac{LFP_{n-1,t} - 2 * LFP_{n,t} + LFP_{n+1,t}}{\Delta z^2}$$

where $LFP_{n,t}$ is the potential sampled on the silicon probe contact n at time t, $LFP_{n-1,t}$, and $LFP_{n+1,t}$ are the potential sampled from the neighboring contacts at time t, and Δz is the spacing between silicon probe contacts, (Bragin et al., 1995; Mitzdorf, 1985). All subsequent transformations were performed on the CSD traces yielded.

We tentatively aligned the silicon probe contacts to the CA1 layers based on LFP observations (Buzsaki, 2002; Mizuseki et al., 2011) and identified periods of theta oscillations (based on LFP from a contact with high amplitude theta oscillations in stratum pyramidale, oriens or radiatum) and start, center and end times of sharp-wave/ripple (90-200 Hz in anesthetized and 130 - 250 Hz in head-fixed; SWR) complexes in the pyramidal layer (described in detail in Lasztoczi et al., 2011 and Lapray et al., 2012). We calculated time-frequency-LFP amplitude plots for each silicon probe contact for each SWR by windowed (centered on the SWR, and time normalized to its duration) extraction of wavelet amplitudes (50 logarithmically equidistant frequencies between 75 and 200 Hz, complex Morlet wavelet with parameters 1 and 1.5), averaged the plots across the SWRs and normalized each frequency separately to the pre-SWR level (Figure S1). The peak increase (per contact) had a characteristic profile across the layers, which was fit with a Gaussian, the centre of which was assumed to be the middle of the stratum pyramidale (Mizuseki et al., 2011). The distance of each contact from the middle of stratum pyramidale was inferred (negative values are dorsal), and the position of each contact with respect to CA1 layers was determined based on boundaries recorded from the 70 µm thick brain section containing the electrode track close to stratum pyramidale (Figure S1).

Histology and 3D reconstruction

Fixation, sectioning, histological procedures, antibodies and analysis of immunohistochemical reactions have been described in detail elsewhere (Lapray et al., 2012; Lasztoczi et al., 2011; Tukker et al., 2013), and are given here in short. More than 1/2 h after the labeling, animals were intra-cardially perfused with fixative (4 % paraformaldehyde, 0.05 % glutaraldehyde, 15 % saturated picric acid), and blocks containing the right hippocampus were sectioned (coronal) with a vibratome (70 µm thickness). Protein expression was tested with multiple immunofluorescent reactions, with antibodies against PV (mouse monoclonal, Swant, 1:5000; guinea-pig, Synaptic Systems, 1:2000), Neuropeptide Y (rabbit, Diasorin-Immunostar, 1:5000), Somatostatin (mouse, Gene Tex, 1:500), α1 subunit of the $GABA_A$ receptor (rabbit, 1:250, gift from Prof. Werner Sieghart), calbindin (rabbit, Swant, 1:5000) and Erb4 (mouse monoclonal, 1:250, Thermo Scientific, code: MS-270-P) and evaluated by epifluorescence microscopy. Specificity of these antibodies is discussed in “our Refs”.

We reconstructed one neurobiotin labeled PV+ basket cell together with the position of the silicon probe, from experiment B96b, with Neurolucida (MBF Bioscience) system mounted on an

Olympus BX 51 microscope, using an UPlanFL N 100x oil immersion objective (NA 1.3). The dendritic arbor was reconstructed in full from six sections of 70 um thickness. All axon in the section containing the soma of the cell was reconstructed. In both rostral and caudal direction branches of main axon in stratum radiatum were followed and reconstructed (with all connected collaterals) until they entered pyramidal layer. Terminal axon branches near the silicon probe track were also reconstructed to show the distance of the silicon probe from the axonal cloud; in total partial axon was reconstructed from 9 sections. The track of silicon probe was reconstructed from 5 sections. All sections were expanded to 70 μm in the Z-direction, and were adjusted (except one reference section, with freeze-thaw permeabilization) in the X-Y plane so that the dendrite endings in neighboring sections match. After the processes were connected, the 3 D reconstruction was expanded in Z and X-Y directions to account for the shrinkage that occurred during processing and fixation (Kisvarday and Eysel, 1993; Tukker et al., 2013) and a schematic model of the silicon probe was inserted so that the individual contacts are in the previously determined radial position. This 3D reconstruction was rotated around the horizontal axis to obtain maximum layer boundary overlap, and is displayed in 2D in Figure 2B.

Statistics and calculus

All calculations were made in Spike2 (CED) and MATLAB (v7.9 - R2009b - 64bit; The Math Works Inc.) by self-developed scripts, functions included in the software (including the Statistics, Signal Processing and the Wavelet toolboxes of MATLAB) or functions from the Circular Statistics Toolbox (Berens, 2009). We used standard statistical procedures to test significance with $\alpha = 0.05$. Values displayed and reported are mean ± SD or circular mean ± circular SD, as appropriate.

SUPPLEMENTARY REFERENCES

Berens, P. (2009). CircStat: A MATLAB Toolbox for Circular Statistics. Journal of Statistical Software *31*, 1-21.
Buzsaki, G. (2002). Theta oscillations in the hippocampus. Neuron *33*, 325-340.
Kisvarday, Z.F., and Eysel, U.T. (1993). Functional and structural topography of horizontal inhibitory connections in cat visual cortex. Eur J Neurosci *5*, 1558-1572.
Csicsvari, J., Henze, D.A., Jamieson, B., Harris, K.D., Sirota, A., Bartho, P., Wise, K.D., and Buzsaki, G. (2003). Massively parallel recording of unit and local field potentials with silicon-based electrodes. J Neurophysiol *90*, 1314-1323.
Mitzdorf, U. (1985). Current source-density method and application in cat cerebral cortex: investigation of evoked potentials and EEG phenomena. Physiol Rev *65*, 37-100.
Mizuseki, K., Diba, K., Pastalkova, E., and Buzsáki, G. (2011). Hippocampal CA1 pyramidal cells form functionally distinct sublayers. Nat Neurosci *14*, 1174-1181.
Pinault, D. (1996). A novel single-cell staining procedure performed in vivo under electrophysiological control: morpho-functional features of juxtacellularly labeled thalamic cells and other central neurons with biocytin or Neurobiotin. J Neurosci Methods *65*, 113-136.
Ylinen, A., Bragin, A., Nádasdy, Z., Jandó, G., Szabó, I., Sik, A., and Buzsáki, G. (1995a). Sharp wave-associated high-frequency oscillation (200 Hz) in the intact hippocampus: network and intracellular mechanisms. J Neurosci *15*, 30-46.
Ylinen, A., Soltesz, I., Bragin, A., Penttonen, M., Sik, A., and Buzsaki, G. (1995b). Intracellular correlates of hippocampal theta rhythm in identified pyramidal cells, granule cells, and basket cells. Hippocampus *5*, 78-90.